

# Excited state quantum phase transitions in the bending spectra of molecules

Jamil Khalouf-Rivera<sup>a</sup>, Francisco Pérez-Bernal<sup>a,b</sup>, Miguel Carvajal<sup>a,b</sup>

<sup>a</sup>*Dpto. Ciencias Integradas, Facultad de Ciencias Experimentales, Centro de Estudios Avanzados en Física, Matemáticas y Computación, Unidad Asociada GIFMAN, CSIC-UHU, Universidad de Huelva, Spain*

<sup>b</sup>*Instituto Universitario Carlos I de Física Teórica y Computacional, Universidad de Granada, Spain*

---

## Abstract

We present an extension of the Hamiltonian of the two dimensional limit of the vibron model encompassing all possible interactions up to four-body operators. We apply this Hamiltonian to the modeling of the experimental bending spectrum of fourteen molecules. The bending degrees of freedom of the selected molecular species include all possible situations: linear, bent, and nonrigid equilibrium structures; demonstrating the flexibility of the algebraic approach, that allows for the consideration of utterly different physical cases with a general formalism and a single Hamiltonian. For each case, we compute predicted term values used to depict the quantum monodromy diagram, the Birge-Sponer plot, the participation ratio. We also show the bending energy functional obtained using the coherent –or intrinsic– state formalism.

**Keywords:** Nonrigid molecules, linear molecules, quasilinear molecules, bent molecules, bending rovibrational structure, algebraic Vibron Model

---

## 1. Introduction

The two-dimensional nature of the vibrational bending degree of freedom, despite having two well-known physical limits as the linear and bent molecular equilibrium structures, implies rovibrational couplings in quasilinear systems that have been the source of frequent misunderstandings, even for triatomic systems, in the description of the molecular bending dynamics [1]. If the potential energy surface associated with a particular system has its minimum in the origin (i.e. it coincides with the molecular axis) the system is said to be linear. If this minimum is replaced by a maximum, and the potential minimum

---

*Email addresses:* [yamil.khalouf@dc1.uhu.es](mailto:yamil.khalouf@dc1.uhu.es) (Jamil Khalouf-Rivera), [francisco.perez@dfaie.uhu.es](mailto:francisco.perez@dfaie.uhu.es) (Francisco Pérez-Bernal), [miguel.carvajal@dfa.uhu.es](mailto:miguel.carvajal@dfa.uhu.es) (Miguel Carvajal)



is located somewhere else, the molecule is said to have a bent equilibrium structure. Of course, this is not always so simple –even for textbook examples with a linear configuration [2]– and, apart from the two well-defined limiting cases, one often has to deal with quasilinear molecules, whose bending dynamics is characterized by large amplitude nuclear displacements and lie very far from the traditional normal mode approach realms. The variety of possible cases can be clearly illustrated by correlation energy diagrams that follow the evolution of energy levels from one limiting case to the other [3; 4].

For quasilinear molecular species, we make a further distinction in the present work between *quasilinear* and *nonrigid* molecules. The quasilinear case has a molecular bending potential with a flat minimum at the origin, and its bending spectrum has peculiar signatures, e.g., a positive anharmonicity in the Birge-Sponer plot or an anomalous ordering of the energy levels –with maximum vibrational angular momentum levels at lower energies for a given number of quanta of vibration. The nonrigid case is even richer in spectroscopic signatures, and it happens once the bending excitation energy reaches values high enough to allow the vibrational bending wave function to explore the linear configuration, which in principle is classically forbidden due to the existence of the barrier to linearity. This explains the switch between negative and positive anharmonicities in the Birge-Sponer plot that characterizes these molecules, the well-known Dixon dip [5]. Of course, as we will later explain, whether a molecule is considered as nonrigid or not, may depend on the advance of experimental techniques that facilitate the access to bending excited states at energies around the barrier to linearity.

The study of large amplitude bending dynamics, and the ensuing coupling between vibrational and rotational degrees of freedom, has been successfully carried out making use of different approaches. Most of them solve a zeroth-order Hamiltonian, where the large amplitude motion (LAM) is placed on equal footing with rotations, and then consider the complete vibrational-rotational Hamiltonian with respect to a configuration of reference. Perfect examples of this philosophy are the bender Hamiltonian of Hougen-Bunker-Johns [6], its extensions, like the semirigid bender Hamiltonian [7] and the general semirigid bender Hamiltonian [8], or the MORBID [9] model.

The barrier to linearity in nonrigid species is modeled with Mexican-hat type potentials. Such potentials classically prevent the definition of global action variables [10]. When this situation is considered from the point of view of quantum mechanics, it translates into the impossibility of finding a unique set of quantum labels globally valid for the system [11]. The access to the classically forbidden origin for increasing excitation energies gives birth to the phenomenon of *quantum monodromy*, introduced by Child, and characterized by a piling of states around a critical energy value and a particular dependence of the bending energy levels on the vibrational angular momentum, evinced in the quantum monodromy diagram [11]. This feature was soon used as an effective tool for the labeling of highly excited energy levels of water in particularly difficult energy regions [12], and quantum monodromy signatures have been later found in other molecular species [13; 14; 15; 16; 17].



The present work is based on an algebraic approach that treats quantum many-body systems with  $N$  degrees of freedom in terms of bosonic realizations of the  $U(N + 1)$  Lie algebra [18]; an approach that has proved successful in modeling the structure of widely different systems: nuclei [19; 20], hadrons [21], and molecules [22]. In the latter case, the model has been called the *vibron model*, and it treats rovibrational excitations in molecules as collective bosonic excitations (*vibrons*). Originally introduced by Iachello for the study of the full rovibrational spectrum of diatomic molecular species [23] and based on the  $U(4)$  Lie algebra, this model was later extended to model the spectrum of tri- [24] and tetratomic [25] molecular species. We use the two-dimensional limit of the vibron model (2DVM), with a  $U(3)$  dynamical algebra, originally introduced for the study of single and coupled benders [26]. This model provides an effective Hamiltonian able to deal with bending large amplitude motions and couplings with the rotational projection around the molecule-fixed z-axis. The model allows for a simple, though complete, description of the linear and bent limiting cases, as well as of the quasilinear and nonrigid regimes [27; 28]. A thorough description of the model can be found in Ref. [29].

A point of particular interest in the case of algebraic models is the study of ground state quantum phase transitions (QPTs), zero-temperature transitions between phases associated with specific configurations of the system ground state. The different phases are often associated with well-known limits, called *dynamical symmetries*. These transitions are non-thermal and are driven through the variation of one or several Hamiltonian parameters (control parameters). The study of such transitions can be traced back to the seminal studies of Gilmore [30] and it has received a great deal of attention in algebraic models of nuclear structure [31; 32; 33]. The description of the ground state QPT for the 2DVM model is detailed in Ref. [29]. Other aspects of interest about this transition can be found in Refs. [34; 35; 36; 37; 38; 39].

More recently, the ground state QPT concept has been extended to the realm of excited states, with the introduction of excited state quantum phase transitions (ESQPTs), where a singularity in the energy spectrum happens due to the clustering of excited levels at a certain critical energy [40; 41]. This critical point can be reached in two different ways: by the variation of a Hamiltonian control parameter for a constant excitation energy or by the increase of the excitation energy for a Hamiltonian with constant parameters (in a certain control parameters range). ESQPTs have been studied in different quantum systems, e.g., the nuclear interacting boson [31], Jaynes-Cummings [42], kicked-top [43], Lipkin-Meshkov-Glick (LMG) [31; 44; 45], and Dicke [35; 42; 46] models.

In the molecular case, it was shown that quantum monodromy and its associated clustering of excited levels can be understood as a manifestation of an ESQPT [29] and it can be understood from a common formulation applied to other many-body systems [40; 47]. In fact, as the 2DVM is the simplest two-level bosonic model with a non-trivial angular momentum, it has been often used to illustrate the occurrence of ESQPTs in algebraic models [41; 48; 49]. Due to the experimental advances that have made possible to record highly-excited bending overtones in nonrigid systems, the molecular bending degree of freedom has



been the first quantum system where experimental signatures of ESQPTs have been found [13; 14] and explained from an algebraic perspective [50; 51]. Other systems where experimental access to ESQPTs have been achieved are superconducting microwave billiards [52] and spinor condensates [53]. The authors and Santos have recently shown evidences of a link between the ESQPT formalism and the study of the transition state in isomerization chemical reactions [54].

The present work can be considered as an extension and an update of the results presented in [50] and [51]. In these two works particular bending modes of several molecular species with different characteristics –linear, quasilinear, non-rigid and bent– were modeled making use of the 2DVM. The selected species are mostly four- or five-atomics in [50] and triatomics in [51]. Their bending rovibrational structure was explained in terms of the most general 2DVM Hamiltonian up to two-body interactions (besides the water molecule case, where extra interactions were taken into consideration). In the present work, we extend the number of interactions and make use of the most general 2DVM Hamiltonian that includes all possible interactions up to four-body. We have revisited the 26 molecules studied in [50; 51], updated the experimental dataset whenever new data are available. We have found that in ten cases the results can be improved –in some of them to a great extent– with the four-body Hamiltonian. In addition to this we also have added to the study the experimental bending spectrum for two nonrigid species ( $\text{Si}_2\text{C}$  and  $\text{OCCCO}$ ) and two bent molecules ( $\text{SiH}_2$  and  $\text{O}_3$ ).

In summary, fourteen molecular species, which can be classified as linear or quasilinear, nonrigid, and bent molecules, have been analyzed. There are four linear and quasilinear molecules: fulminic acid ( $\text{HCNO}$ ), hydrogen cyanide ( $\text{HCN}$ ), hydrogen isocyanide ( $\text{HNC}$ ), and cyanofulminate ( $\text{NCCNO}$ ). The number of nonrigid molecules included in the study is six, all of them with distinctive signatures of ESQPT in their spectra: methyl isocyanate ( $\text{CH}_3\text{NCO}$ ), isothiocyanic acid ( $\text{HNCS}$ ), cyanogen isothiocyanate ( $\text{NCNCS}$ ), the isotopologue  $^{37}\text{Cl}$  of chloronitrile oxide ( $^{37}\text{ClCNO}$ ), carbon suboxide ( $\text{OCCCO}$ ), and disilicon carbide ( $\text{Si}_2\text{C}$ ). Finally, we have also included in the analysis data for four bent molecules: hydrogen sulfide ( $\text{H}_2\text{S}$ ), hydrogen selenide ( $\text{H}_2\text{Se}$ ), silylene ( $\text{SiH}_2$ ), and ozone ( $\text{O}_3$ ).

In addition to the resulting calculated spectra and spectroscopic parameters for the selected species, making use of the optimized wave functions, we have also computed the participation ratio [55] for all the molecules examined in the two bases of the 2DVM that can be mapped to the linear and bent limiting cases [29]. The participation ratio is a quantity that recently has been shown to detect in systems with an ESQPT a strong localization in the eigenstates with energies close to the critical energy of the ESQPT [49; 56; 57]. This fact has important effects in the system dynamics and it has been proved in the vibron model [56], as well as in its two- [49], and one-dimensional limits [57].

Finally, we make use of the coherent or intrinsic state formalism [29; 58; 59] to compute, making use of the optimized spectroscopic parameters, an approximation to the system bending energy functional and, in nonrigid cases, to the



value of the barrier to linearity.

## 2. The two dimensional limit of the vibron model

The 2D limit of the vibron model, the 2DVM, was introduced in Ref. [26]. Since then, it has been applied to model molecular bending degrees of freedom due to its general character, able to encompass the two limiting linear and bent molecular structures and the interesting situations in-between them. In the field of molecular structure, the model was applied to different problems involving bending vibrations: calculation of infrared transition intensities [60; 61], definition of an algebraic force field for bending vibrations [62], computation of Franck-Condon factors [63], characterizing signatures of non-rigidity in energy spectra [27], and modeling dipole or Raman line intensities [28; 64; 65; 66]. Somewhat different alternative algebraic approaches to molecular structure that try to get a firm grasp on the connection to the traditional phase space approach are also based on the 2DVM [67; 68; 69]. More recently, inspired by the use of spectroscopic information to characterize the transition state in isomerization reactions presented in Ref. [70], the authors have found that the 2DVM model is specially fit to reproduce the transition state energy in such reactions, applying this finding to the system HCN-HNC [54].

Specially important for the present discussion are Refs. [50; 51], where a careful study of many different benders is presented and the model results are explained under the prism of the occurrence of an ESQPT in nonrigid cases. We also make extensive use of the detailed description of the model provided in Ref. [29].

It is worth to mention the efforts to apply the model to situations where two benders are coupled, which implies a significantly larger computational complexity and where the obtained results can be understood considering from the perspective of QPTs involving two bosonic fluids [71; 72; 73; 74; 75]. Related to this, we would also like to mention the use of the 2DVM model in the study of the spectra of 2D crystals with different lattice geometry [76].

The 2DVM associates a  $U(3)$  dynamical algebra to each bender, and builds the system Hamiltonian as a expansion in terms of operators, with the right symmetry properties, belonging to the dynamical algebra or to its subalgebras. The interested reader can find a detailed mathematical description of the model in Refs. [26; 29]. We provide here some basic details concerning the bases and Hamiltonians we use in the present work and we also introduce the participation ratio, a quantity used to analyze the wave function localization in the different bases, and we make a short stroll into the classical limit of the model obtained using the intrinsic state formalism.

### 2.1. The cylindrical and displaced oscillator bases

There are two possible subalgebra chains starting from the dynamical algebra,  $U(3)$ , and ending in the system symmetry algebra,  $SO(2)$ . The requirement



of having  $SO(2)$  as the symmetry algebra implies angular momentum conservation in the system [77]

$$\begin{array}{ccccc}
 & & U(2) & & Chain(I) \\
 & \nearrow & & \searrow & \\
 U(3) & & & & SO(2) \\
 & \searrow & & \nearrow & \\
 & & SO(3) & & Chain(II)
 \end{array} \quad (Eq. 1)$$

Each one of the possible subalgebra chains, known as a *dynamical symmetry*, provides an analytical solution to the problem, an energy formula, and can be mapped to certain physical cases [18; 77]. In addition to this, there is a set of quantum labels and therefore, a basis, associated with every dynamical symmetry. We proceed to detail the basis quantum numbers and branching rules for the two dynamical symmetries at stake.

*The cylindrical oscillator basis.* The  $U(3) \supset U(2) \supset SO(2)$  chain is known as the cylindrical oscillator chain and it corresponds to the linear case. Its states are labeled by the quantum numbers  $n$  and  $\ell$

$$\left| \begin{array}{c} U(3) \supset U(2) \supset SO(2) \\ [N] \quad n \quad \ell \end{array} \right\rangle, \quad (Eq. 2)$$

and the associated basis states are denoted as  $|[N]; n^\ell\rangle$ . The quantum number  $N$  labels the totally symmetric representation of  $U(3)$ . The total number of bound states of the system is a function of  $N$ . The label  $n$  is the vibrational quantum number and  $\ell$  is the vibrational angular momentum. The branching rules in this case are

$$\begin{aligned}
 n &= N, N-1, N-2, \dots, 0 \\
 \ell &= \pm n, \pm(n-2), \dots, \pm 1 \text{ or } 0, \quad (n = \text{odd or even}) \quad . \quad (Eq. 3)
 \end{aligned}$$

This is the most convenient basis to fit experimental bending vibration data in the case of linear and quasilinear molecules. We provide in Appendix A.0.1 the matrix elements in this basis of the different operators included in the 2DVM Hamiltonian.

*The displaced oscillator basis.* States in the displaced oscillator chain, associated to the bending in molecules with a bent geometric configuration, are characterized by the quantum numbers

$$\left| \begin{array}{c} U(3) \supset SO(3) \supset SO(2) \\ [N] \quad \omega \quad \ell \end{array} \right\rangle. \quad (Eq. 4)$$

and will be denoted as  $|[N]; \omega, \ell\rangle$ . The branching rules are

$$\begin{aligned}
 \omega &= N, N-2, N-4, \dots, 1 \text{ or } 0, \quad (N = \text{odd or even}), \\
 \ell &= \pm\omega, \pm(\omega-1), \dots, 0 \quad . \quad (Eq. 5)
 \end{aligned}$$



In this case, it is convenient to introduce a vibrational quantum number  $\nu_b$ , which can be identified with the number of quanta of excitation in the displaced oscillator:

$$\nu_b = \frac{N - \omega}{2} . \quad (\text{Eq. 6})$$

The branching rules in this case are

$$\begin{aligned} \nu_b &= 0, 1, \dots, \frac{N-1}{2} \text{ or } \frac{N}{2}, \quad (N = \text{odd or even}), \\ \ell &= 0, \pm 1, \pm 2, \dots, \pm(N - 2\nu_b) . \end{aligned} \quad (\text{Eq. 7})$$

This is the natural basis to fit experimental bending vibration data in the case of nonrigid and bent molecules. We provide in Appendix A.0.2 the matrix elements in this basis of the different operators in the four-body 2DVM Hamiltonian.

## 2.2. The 2DVM Hamiltonian

In this work we make use of three different Hamiltonian operators of increasing complexity. The simplest one,  $\hat{\mathcal{H}}$ , which has been chiefly used in the study of ground and excited state QPTs in the 2DVM, is a very simplified Hamiltonian, that includes the  $\hat{n}$  operator from the cylindrical oscillator dynamical symmetry and the Pairing operator  $\hat{P}$  from the displaced oscillator dynamical symmetry. The Pairing operator is  $\hat{P} = N(N+1) - \hat{W}^2$  [29].

$$\hat{\mathcal{H}} = \varepsilon \left[ (1 - \xi)\hat{n} + \frac{\xi}{N-1}\hat{P} \right] . \quad (\text{Eq. 8})$$

This Hamiltonian has two parameters: a global energy scale  $\varepsilon$  and a control parameter  $\xi$ . For  $\xi = 0.0$  the system is in the first dynamical symmetry and for  $\xi = 1.0$  the system is in the second one. This is specially adequate to characterize the ground and excited state QPTs, with second order ground state QPT for the critical value  $\xi_c = 0.2$  [29]. In the present work we use this Hamiltonian to illustrate the use of the participation ratio to evince the ESQPT.

A second Hamiltonian of interest is  $\hat{H}_{2b}$ , the most general one- and two-body Hamiltonian of the 2DVM [26; 29]

$$\hat{H}_{2b} = E_0 + \epsilon\hat{n} + \alpha\hat{n}(\hat{n}+1) + \beta\hat{\ell}^2 + A\hat{P} , \quad (\text{Eq. 9})$$

where the operators  $\hat{n}$  and  $\hat{n}(\hat{n}+1)$  are Casimir operators of the cylindrical oscillator chain, the pairing operator  $\hat{P}$  is the Casimir operator of the displaced oscillator chain, and the vibrational angular momentum,  $\hat{\ell}$ , is common to both dynamical symmetries. In fact, in all the considered cases, the angular momentum is a constant of the motion, i.e.,  $\ell$  is a good quantum number, and the Hamiltonian matrix is block diagonal in  $\ell$ , a fact that simplifies the numerical calculations reducing the dimension of the considered matrices. This reduction is further increased as for  $\ell \neq 0$  only positive angular momentum values are considered. This is explained because, in absence of external fields, the first



order angular momentum operator  $\hat{\ell}$  is not included and there is a degeneracy between positive and negative  $\ell$  values.

The third Hamiltonian considered is  $\hat{H}_{4b}$ , the most general 1-, 2-, 3-, and 4-body Hamiltonian expressed as follows

$$\begin{aligned}
\hat{H}_{4b} = & P_{11}\hat{n} \\
& + P_{21}\hat{n}^2 + P_{22}\hat{\ell}^2 + P_{23}\hat{W}^2 \\
& + P_{31}\hat{n}^3 + P_{32}\hat{n}\hat{\ell}^2 + P_{33}(\hat{n}\hat{W}^2 + \hat{W}^2\hat{n}) \\
& + P_{41}\hat{n}^4 + P_{42}\hat{n}^2\hat{\ell}^2 + P_{43}\hat{\ell}^4 + P_{44}\hat{\ell}^2\hat{W}^2 \\
& + P_{45}(\hat{n}^2\hat{W}^2 + \hat{W}^2\hat{n}^2) + P_{46}\hat{W}^4 + P_{47}(\hat{W}^2\hat{\bar{W}}^2 + \hat{\bar{W}}^2\hat{W}^2)/2 .
\end{aligned} \tag{Eq. 10}$$

This Hamiltonian has fourteen spectroscopic constants  $P_{ij}$ , where the subindexes indicate that the parameter is the  $j$ -th operator among the  $i$ -body operators.

From the matrix elements of the creation and annihilation sigma and  $\tau$  bosons in the two bases associated with the model dynamical symmetries, published in [29], the operator matrix elements of all operators in Eq. 10 can be derived. We provide the matrix elements of the operators in the two bases of interest as an appendix to the present work.

### 2.3. ESQPT and Participation Ratio

It has been recently shown that in all vibron model limits the ESQPT occurring between the  $U(N-1)$  and  $SO(N)$  dynamical symmetries (for  $N=2,3,4$ ) implies a strong localization of the wave function for the state(s) closer to the critical energy of the transition when expressed in the  $U(N-1)$  basis. This fact has important consequences in the system dynamics [49; 56; 57]. A convenient quantity to reveal this localization, closely related to the Shannon information entropy [78], is the participation ratio (PR) [55]. This quantity is also named inverse participation ratio [79] or number of principal components [78]. If we consider a basis  $\{|\psi_i\rangle\}_{i=1}^{dim}$ , we can express the eigenstates of our problem as  $|\Psi_k\rangle = \sum_{i=1}^{dim} c_{ki} |\psi_i\rangle$ , with the usual normalization  $\sum_{i=1}^{dim} c_{ki} c_{k'i}^* = \delta_{k'k}$ . The PR is defined as the inverse of the sum of  $c_{ki} c_{ki}^*$  squared:

$$PR[\Psi_k] = \frac{1}{\sum_{i=1}^{dim} |c_{ki}|^4} . \tag{Eq. 11}$$

The minimum value of the PR for a given state is one, when the eigenfunction corresponds exactly with a basis state and all  $c_{ki}$  components are zero besides one which is equal to unity. This entails a maximum localization in the selected basis. On the other hand, the maximum value of the PR is  $dim$ , the dimension of the Hamiltonian block. This value is attained once the wavefunction has all their components equal and non-zero. In the present case we can express eigenstates



in one of the two bases associated with the  $U(3)$  dynamical symmetries

$$\begin{array}{c}
 \left| \Psi_k^{(\ell)} \right\rangle \begin{array}{l} \nearrow \\ \searrow \end{array} \begin{array}{l} \left| \Psi_k^{(\ell)} \right\rangle = \sum_n c_{kn}^{(\ell)} |[N]; n^\ell \rangle \quad (\text{Cylindrical oscillator chain}) \\ \left| \Psi_k^{(\ell)} \right\rangle = \sum_{\nu_b} d_{k\nu_b}^{(\ell)} |[N]; \nu_b \ell \rangle \quad (\text{Displaced oscillator chain}). \end{array}
 \end{array}
 \tag{Eq. 12}$$

PR values are usually normalized, dividing the value obtained from (Eq. 12) by the dimension of the space. This facilitates the comparison for systems with different sizes. The results obtained for the model Hamiltonian (Eq. 8) help to illustrate the information provided by the PR quantity. The ground state QPT for the model Hamiltonian happens for the critical control parameter value  $\xi_c = 0.2$  and the ESQPT occurs for control parameters values larger than  $\xi_c$ , at increasing energy values. The ESQPT is marked by a nonanalyticity of the energy level density at the critical energy in the thermodynamic or mean field limit ( $N \rightarrow \infty$ ). In Fig. 1 we depict the correlation energy diagram for  $N = 2000$  and  $0 \leq \xi \leq 1$  and we plot the PR for the cylindrical (left panel) and displaced (right panel) oscillator basis as a heat map. The left panel shows the high localization of the states on the separatrix that marks the ESQPT (low PR values) when expressed in the cylindrical oscillator basis. States located above the separatrix have a  $U(2)$  character –being closer to a linear configuration– while states below the separatrix have a  $SO(3)$  character –closer to a bent configuration.



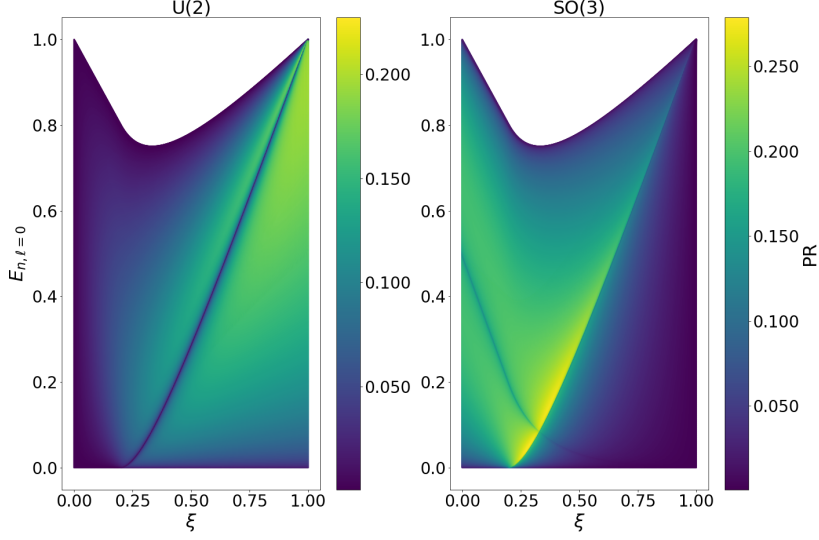


Figure Fig. 1: Both panels represent the normalized excitation energies for  $\ell = 0$  states with  $N = 2000$  versus the  $\xi$  parameter of the model Hamiltonian (Eq. 8). Each energy point is colored in accordance with the eigenstate normalized PR in the cylindrical oscillator (left panel) or the displaced oscillator (right panel) basis.

#### 2.4. Mean field limit of the 2DVM

The zero temperature ground and excited state QPTs truly occur in the thermodynamic limit –or mean field limit– of the system, for large system sizes (large  $N$  values). In any case, the derivation of a classical energy functional from the algebraic Hamiltonian is of great help in understanding and classifying these phenomena. A classical energy functional, within a  $1/N$  approximation, can be obtained with the coherent or intrinsic state formalism. This formalism, originally introduced by Gilmore [30], was applied at first hand to algebraic models in nuclear physics [58], and later extended to molecular systems [59]. We present here the basic results, further details about the intrinsic state formalism results for the 2DVM model can be found in Ref. [29].

The initial step is the consideration of the coherent (or intrinsic) ground state

$$|[N]; \mathbf{r}\rangle = \frac{1}{\sqrt{N!}} (b_c^\dagger)^N |0\rangle, \quad (\text{Eq. 13})$$

that is normalized, and where  $\mathbf{r}$  stands for the 2D classical coordinates and  $b_c^\dagger$  is the boson condensate operator

$$b_c^\dagger = \frac{1}{\sqrt{1+r^2}} [\sigma^\dagger + x\tau_x^\dagger + y\tau_y^\dagger]. \quad (\text{Eq. 14})$$



Calculating the expectation value of the Hamiltonian (Eq. 10) in the coherent state (Eq. 13) we obtain the system energy functional  $E(r)$

$$E(r) = \langle [N]; \mathbf{r} | \hat{H}_{4b} | [N]; \mathbf{r} \rangle \quad (\text{Eq. 15})$$

The results for the different terms composing the four-body algebraic Hamiltonian (Eq. 10) is

- **One body operator:**

$$\circ \langle \hat{n} \rangle_{c.s.} = N \frac{r^2}{1+r^2}$$

- **Two body operators:**

$$\circ \langle \hat{n}^2 \rangle_{c.s.} = N \frac{r^2}{1+r^2} + N(N-1) \frac{r^4}{(1+r^2)^2}$$

$$\circ \langle \hat{\ell}^2 \rangle_{c.s.} = \langle \hat{n} \rangle_{c.s.}$$

$$\circ \langle \hat{W}^2 \rangle_{c.s.} = 2N + N(N-1) \frac{4r^2}{(1+r^2)^2}$$

- **Three body operators:**

$$\circ \langle \hat{n}^3 \rangle_{c.s.} = N \frac{r^2}{1+r^2} + 3N(N-1) \frac{r^4}{(1+r^2)^2} + N(N-1)(N-2) \frac{r^6}{(1+r^2)^3}$$

$$\circ \langle \hat{n} \hat{\ell}^2 \rangle_{c.s.} = \langle \hat{n}^2 \rangle_{c.s.}$$

$$\circ \langle \hat{n} \hat{W}^2 + \hat{W}^2 \hat{n} \rangle_{c.s.} = 4N \frac{r^2}{1+r^2} + 4N(N-1) \frac{r^4}{(1+r^2)^2} + 12N(N-1) \frac{r^2}{(1+r^2)^2} + 8N(N-1)(N-2) \frac{r^4}{(1+r^2)^3}$$

- **Four body operators:**

$$\circ \langle \hat{n}^4 \rangle_{c.s.} = N \frac{r^2}{1+r^2} + 7N(N-1) \frac{r^4}{(1+r^2)^2} + 6N(N-1)(N-2) \frac{r^6}{(1+r^2)^3} + N(N-1)(N-2)(N-3) \frac{r^8}{(1+r^2)^4}$$

$$\circ \langle \hat{n}^2 \hat{\ell}^2 \rangle_{c.s.} = \langle \hat{n}^3 \rangle_{c.s.}$$

$$\circ \langle \hat{\ell}^4 \rangle_{c.s.} = N \frac{r^2}{1+r^2} + 3N(N-1) \frac{r^4}{(1+r^2)^2}$$

$$\circ \langle \hat{\ell}^2 \hat{W}^2 \rangle_{c.s.} = 2N \frac{r^2}{1+r^2} + 4N(N-1) \frac{r^4+r^2}{(1+r^2)^2} + 4N(N-1)(N-2) \frac{r^4}{(1+r^2)^3}$$

$$\circ \langle \hat{n}^2 \hat{W}^2 + \hat{W}^2 \hat{n}^2 \rangle_{c.s.} = 4N \frac{r^2}{1+r^2} + N(N-1) \frac{12r^4+16r^2}{(1+r^2)^2} + N(N-1)(N-2) \frac{4r^6+28r^4}{(1+r^2)^3} + N(N-1)(N-2)(N-3) \frac{8r^6}{(1+r^2)^4}$$

$$\circ \langle \hat{W}^4 \rangle_{c.s.} = 4N(2N-1) + 24N(N-1) \frac{r^2}{(1+r^2)^2} + 32N(N-1)(N-2) \frac{r^4+r^2}{(1+r^2)^3} + 16N(N-1)(N-2)(N-3) \frac{r^4}{(1+r^2)^4}$$

$$\circ \frac{1}{2} \langle \hat{W}^2 \hat{\bar{W}}^2 + \hat{\bar{W}}^2 \hat{W}^2 \rangle_{c.s.} = 4N + N(N-1) \frac{4r^4+28r^2}{(1+r^2)^2} + 8N(N-1)(N-2) \frac{r^4+r^2}{(1+r^2)^3}$$



• **Six body operator:**

$$\begin{aligned} \text{o } \left\langle \hat{\ell}^4 \hat{W}^2 \right\rangle_{c.s.} &= N \frac{2r^2}{1+r^2} + N(N-1) \frac{22r^4+4r^2}{(1+r^2)^2} + N(N-1)(N-2) \frac{18r^6+22r^4}{(1+r^2)^3} \\ &\quad + N(N-1)(N-2)(N-3) \frac{12r^6}{(1+r^2)^4} \end{aligned}$$

We have included a single six-body term that has been used exclusively to improve the fit of the data for the bending of the ozone molecule.

The transformation from the dimensionless variable  $r$ , provided by the intrinsic approach, to the deviation of linearity angle  $\theta$  implies a connection between the physical system and its algebraic realization. This has been previously worked out for the two dynamical symmetries [27; 50]. The use of higher-order terms in the Hamiltonian further complicates this connection and we explain the procedure followed for each type of molecule in the corresponding subsection, 3.1 for linear and quasilinear, 3.2 for bent and 3.3 for nonrigid.

### 3. Results

Probably, the main advantage of the 2DVM is the possibility to encompass, in a computationally simple approach, the full gamut of behaviors expected for molecular bending vibrations: linear or bent semi-rigid configurations and the nonrigid case, characterized by having a large amplitude, highly anharmonic, degree of freedom. This latter possibility is achieved with a Hamiltonian operator that combines interactions inherent to the linear and bent molecules.

In order to display the 2DVM versatility we model bending rovibrational experimental data for three sets of molecules which have very different spectroscopic signatures: (i) Semirigid linear or quasilinear molecules; (ii) semirigid bent molecules; and (iii) nonrigid molecules with a large amplitude bent-to-linear mode. In all cases, the bending spectrum has been reproduced making use of the most general 4-body Hamiltonian (Eq. 10). For this purpose we have collected all the available experimental data, up to our knowledge, for four linear and quasilinear, four bent, and six nonrigid molecular species. Making use of this information, the  $P_{ij}$  spectroscopic parameters of Hamiltonian (Eq. 10) have been optimized and the rovibrational spectra reproduced obtaining a good agreement between calculated and experimental data.

As mentioned above, the present work can be considered as an extension of previous works where most fits were performed with a two-body Hamiltonian [50; 51]. We have reviewed the results obtained in [50; 51] making use of the four-body 2DVM Hamiltonian (Eq. 10) and we report those cases where results have noticeably improved with the addition of operators of three- or four-body character. In such cases the value of the total vibron number,  $N$ , in each case has been fixed to the value published in [50; 51] and we compare the new and former *rms* values. All the interactions from the general 4-body Hamiltonian (Eq. 10) have been used in one case or another, except those with parameters  $P_{41}$  and  $P_{47}$ . Apart from the molecular species already studied in [50; 51], we have included in our analysis data for other four molecular species



(SiH<sub>2</sub>, Si<sub>2</sub>C, OCCCO, and O<sub>3</sub>). In these cases, the total vibron number has been fixed from its effect on the *rms* following the analysis presented in [51].

Apart from the calculation of the fit to the spectrum, we have delved into the dynamical structure of the different molecular systems. We show in all cases the resulting quantum monodromy diagram, Birge-Sponer plot, participation ratio, and classical energy functional. We plot the quantum monodromy diagram and the Birge-Sponer plot including experimental and calculated term values, as well as the algebraic four-body Hamiltonian model predictions for yet unknown energy levels. Tables with the values of the predicted levels can be found in the Supplementary Material. We also plot for the different molecular species the PR for the optimized zero vibrational angular momentum eigenstates as a function of the state energy for the cylindrical (Eq. 2) and the displaced oscillator (Eq. 4) bases. Finally, we also show the energy functional for the modeled bending vibrational degree of freedom obtained with the intrinsic state approach using the optimized spectroscopic parameters as an input.

We have developed a Fortran source code for the calculation of the algebraic Hamiltonian (Eq. 10) as well as the different quantities included in the present work. The code makes use of the LAPACK [80] and LAPACK95 [81] libraries for matrix diagonalization and it also performs the needed state assignment tasks. The parameter optimization procedure is a nonlinear least square fitting through *minuit* Fortran code [82]. The minimization finishes once parameter convergence is reached and a careful check of the obtained parameters has been carried out, to ascertain their physical character. The code is available under request to the authors and it will be published in a forthcoming work [83].

As we are presenting results for several molecular systems, we have organized this section into three subsections. In the first one, we include the results obtained for four linear or quasilinear molecules. The second one is devoted to bent molecules, including other four molecular species. Finally, the third subsection is reserved to nonrigid molecular species, and includes the bending spectrum of six molecules.

### 3.1. Linear and quasilinear molecules

In this subsection we study the bending motion for two triatomic molecules (hydrogen cyanide (HCN) and hydrogen isocyanide (HNC)) as well as the large amplitude bending vibrational mode of a tetratomic (fulminic acid (HCNO)) and a five-atomic molecule (cyanofulminate (NCCNO)). Taking into account the classification sketched in the introduction of this work, all of them can be considered as linear or quasilinear molecules.

The interactions that stem from the cylindrical oscillator subalgebra chain (Eq. 1) are the main ones for linear and quasilinear molecules, although the interaction  $\hat{W}^2$ , from the displaced oscillator chain in (Eq. 1) is also needed. This is specially true for quasilinear molecules, due to the flatness of the potential that characterizes systems close to the ground state QPT [50; 51]. Tab. 1 includes Hamiltonian (Eq. 10) optimized parameter values, the number of experimental term values included in the fit, the total vibron number (N), the *rms* obtained in the present study (*rms<sub>n</sub>*) and the *rms* obtained in previous 2DVM fits (*rms<sub>o</sub>*) [50;



51]. In the HNC case there is a truly remarkable improvement in the *rms*, that can be traced back to the inclusion in the fit of a three-body interaction. There is a slight enhancement for HCN and the results we have obtained for other species included in [50; 51] are comparable to the ones obtained for HCNO, for which the improvement obtained is negligible. Finally, the large amplitude bending mode for NCCNO was not included among the ones studied in Refs. [50; 51].

For linear and quasilinear molecules, we have fixed the abscissa scale in the energy functional in a similar way to Refs. [50; 51]. We connect the deviation-from-linearity angle with the dimensionless coherent intrinsic coordinate assuming a linear relationship  $\theta = \Theta r$ . In our case, the use of high-order operators (e.g.  $\hat{n}\hat{\ell}^2$  and  $\hat{n}^2\hat{\ell}^2$ ) hinders the direct use of parameter  $P_{11}$  in the scaling factor. Therefore, we have used instead the energy of the state with one quantum of vibration, the level  $n = 1$  and  $\ell = 1$ . If  $g$  is the  $g_{33}$  element of the bending  $G$  matrix for triatomic molecules expressed in  $\text{amu}^{-1}\text{\AA}^{-2}$  [84] and  $E_{11}$  is the one quantum term value in  $\text{cm}^{-1}$  units then

$$\Theta = 8.2116 \sqrt{\frac{Ng}{E_{11}}} [\text{rad}] . \quad (\text{Eq. 16})$$

In the case of four- and five-atom molecules, we have kept the triatomic Wilson formula for  $g$ , replacing the corresponding bond lengths and masses by the reduced masses and distances to the center-of-mass of the involved atoms.

Molecule	HCNO	HCN	HNC	NCCNO
$P_{11}$	701(21)	932.5(3)	1414.0(4)	195.7(9)
$P_{21}$	-12.9(15)	-7.649(17)	-29.837(15)	-4.54(6)
$P_{22}$	10.6(7)	6.11(5)	15.81(10)	2.40(5)
$P_{23}$	-7.4(3)	-1.981(3)	-8.054(3)	-1.521(10)
$P_{32}$	-	1.8(5)e-2	4.9(10)e-2	-
$P_{42}$	3(7)e-3	-	-	-
N	24	50	40	28
g	1.1072	1.2001	1.3130	0.1732
$rms_n$	0.08	0.17	0.08	0.27
$rms_o$	0.09	0.7	2.3	-
$N_{data}$	10	30	19	11

Table Tab. 1: Optimized Hamiltonian parameters ( $P_{ij}$ , in  $\text{cm}^{-1}$  units) for linear and quasilinear molecules. Values are given with their associated uncertainty in parentheses in units of the last quoted digits. The total vibron number, the g-matrix element ( $\text{amu}^{-1}\text{\AA}^{-2}$ ) and the *rms* obtained in this work,  $rms_n$ , are also included. For the sake of comparison, the *rms* obtained in Refs. [50; 51], if available, is also shown, labeled as  $rms_o$ .

### 3.1.1. Fulminic Acid, HCNO

We model the  $\nu_5$  quasilinear bending mode of fulminic acid, that has been previously analyzed using the 2DVM [27; 50]. Only ten experimental term values for this mode can be found in the literature [85; 86] and they are used to optimize the Hamiltonian parameters. Despite the known 1:4 Fermi interaction



between the  $\nu_3$  stretching mode and the  $\nu_5^{l_5=0}$  bending mode [85], the calculated energies reproduce the experimental term values within experimental accuracy and the 4-body Hamiltonian (Eq. 10) is a valid effective Hamiltonian for the analysis of this bending mode.

The calculated and experimental energy levels of fulminic acid are both shown in Tab. 2, together with the residual values. These term values, as well as the values predicted by the model, have been used in the setup of Fig. 2. In this figure, the upper left panel is the quantum monodromy plot where the dependence of energy on vibrational angular momentum is approximately linear [87; 88], an expected feature for linear molecules [50].

The top right panel is the Birge-Sponer plot for the mode under study, and the more interesting feature is the positive anharmonicity. We label the abscissa with the bending quantum number  $\nu_b$ , for a set of levels with vibrational angular momentum  $\ell = 0, 1 \dots 5$ . This is in accordance with the fact that, according to model Hamiltonians (Eq. 8 and Eq. 9), this molecule has a quasilinear character [27; 50].

The bottom left panel contains results for the participation ratio where, for levels up to  $2500 \text{ cm}^{-1}$ , the localization is enhanced in the cylindrical oscillator basis set of Eq. 1, as expected for a quasilinear molecule.

Finally, the bottom right panel includes the energy functional obtained using the intrinsic state formalism and the optimized parameter values in Tab. 1 and considering the bond lengths from [15]. It is characterized by a flat minimum, as expected for a bending mode very close to the critical point of the ground state QPT [27; 50]. This agrees very well with the available information on the equilibrium structure of fulminic acid [15], considered as a prototypical example of a quasilinear molecule. The only discrepancy between the obtained results for this molecule and the conclusions drawn in Ref. [15] regards a very modest maximum on the origin for the potential function, which does not appear in [27; 50] either.



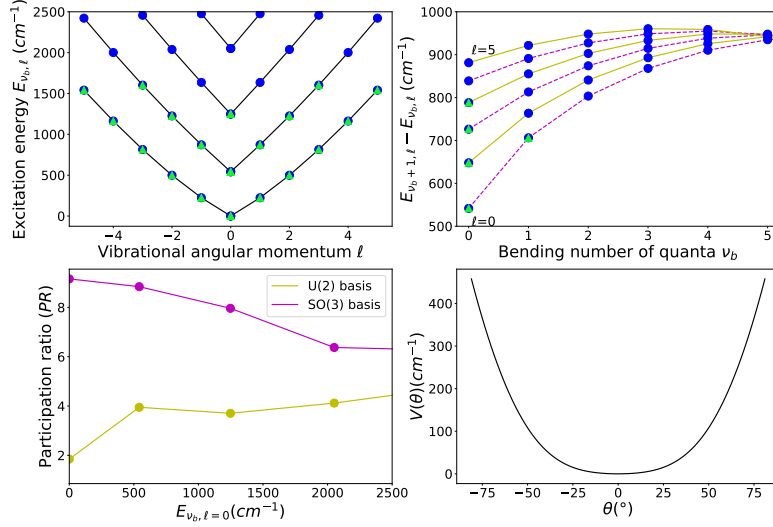


Figure Fig. 2: The upper row includes the quantum monodromy plot (upper left panel) and the Birge-Sponer plot (upper right panel) for the  $\nu_5$  bending mode of HCNO, using blue circles (green triangles) for calculated (experimental) data. The lower row includes the PR for  $\ell = 0$  eigenstates in the two bases considered as a function of the state energy (lower left panel) and the bending energy functional derived using the coherent state formalism (lower right panel).

Table Tab. 2: Experimental and calculated term values and residuals for the  $\nu_5$  bending mode of fulminic acid. Units of  $\text{cm}^{-1}$ .

$(n, \ell)^a$	Exp. <sup>b</sup>	Calc. <sup>c</sup>	Exp.-Calc. <sup>d</sup>
( 2 0)	541.76	541.7216	0.038
( 4 0)	1247.75	1247.8880	-0.138
( 1 1)	224.10	224.0851	0.015
( 3 1)	872.11	872.0560	0.054
( 2 2)	499.06	499.1053	-0.045
( 4 2)	1225.45	1225.3841	0.066
( 3 3)	814.04	814.0616	-0.022
( 5 3)	1602.28	1602.2288	0.051
( 4 4)	1162.66	1162.6336	0.026
( 5 5)	1540.60	1540.6333	-0.033

<sup>a</sup> Cylindrical oscillator basis quantum labels assigned to the optimized eigenvectors.

<sup>b</sup> Experimental energies from Refs. [85; 86].

<sup>c</sup> Calculated energies.

<sup>d</sup> Difference between experimental and calculated energies.



### 3.1.2. Hydrogen Cyanide, HCN

Hydrogen cyanide is a linear triatomic molecule with 30 available experimental energy levels for its single bending mode ( $\nu_2$ ); a set that includes up to 10 quanta of excitation and vibrational angular momentum  $\ell$  up to 9 [89]. All the available experimental values are considered in the fit and the obtained results, together with the experimental values, are included in Tab. 3, where it can be appreciated an excellent agreement between experimental and computed energy term values. In order to improve the results published in [51], the three-body interaction ( $\hat{n}\hat{\ell}^2$ ) of the bending Hamiltonian (Eq. 10) has been included, allowing us to decrease the *rms* from 0.7 to 0.17  $\text{cm}^{-1}$ . Predicted energy levels have been computed from  $\ell = 0$  to 10 and have been used to plot the different panels of Fig. 3.

The quantum monodromy diagram (top left panel) and Birge-Sponer plot (top right panel) clearly agree with a linear equilibrium structure for HCN, with an expected negative anharmonicity for the set of levels with vibrational angular momentum  $\ell = 0$  to 10. These levels are well below the isomerization barrier height. However, using an extended dataset, the 2DVM model has recently proven able to correctly estimate the height of this barrier for the HCN-HNC system [54].

The bottom left panel includes the results for the PR in the two bases considered where it can be easily appreciated how, up to an energy threshold of 12000  $\text{cm}^{-1}$ , eigenstates expressed in the cylindrical oscillator, or  $U(2)$ , chain are more localized than when expressed in the displaced, or  $SO(3)$ , chain. This is the expected result for a linear molecule. The bottom right panel displays the energy functional, confirming the linear geometric equilibrium configuration [90].



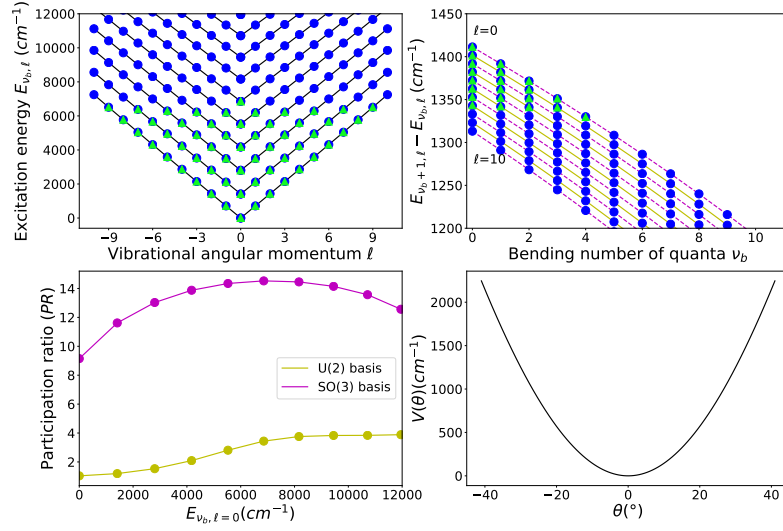


Figure Fig. 3: The upper row shows the quantum monodromy plot (upper left panel) and the Birge-Sponer plot (upper right panel) for the bending mode of HCN with blue circles (green triangles) for predicted (experimental) data. The lower row includes the PR for  $\ell = 0$  eigenstates as a function of the state energy (lower left panel) and the bending energy functional derived using the coherent state formalism (lower right panel).



Table Tab. 3: Experimental and calculated term values and residuals for the bending mode of HCN. Units of  $\text{cm}^{-1}$ .

$(n, \ell)^a$	Exp. <sup>b</sup>	Cal. <sup>c</sup>	Exp.-Cal. <sup>d</sup>
(0 0)	0.00	0.0000	0.000
(2 0)	1411.41	1411.3570	0.053
(4 0)	2802.95	2803.0782	-0.128
(6 0)	4174.60	4174.7140	-0.114
(8 0)	5525.81	5525.7900	0.020
(10 0)	6855.44	6855.8030	-0.363
(1 1)	711.97	711.8211	0.149
(3 1)	2113.28	2113.4616	-0.182
(5 1)	3495.14	3495.2446	-0.105
(7 1)	4856.74	4856.7085	0.032
(9 1)	6197.44	6197.3647	0.075
(2 2)	1426.52	1426.3117	0.208
(4 2)	2818.17	2818.2200	-0.050
(6 2)	4189.97	4190.0432	-0.073
(8 2)	5541.39	5541.3069	0.083
(3 3)	2143.75	2143.5585	0.191
(5 3)	3525.64	3525.7160	-0.076
(7 3)	4887.52	4887.5549	-0.035
(9 3)	6228.58	6228.5870	-0.007
(4 4)	2863.78	2863.6472	0.133
(6 4)	4236.01	4236.0326	-0.023
(8 4)	5588.00	5587.8594	0.141
(5 5)	3586.69	3586.6624	0.028
(7 5)	4949.31	4949.2515	0.059
(9 5)	6291.32	6291.0352	0.285
(6 6)	4312.62	4312.6876	-0.068
(8 6)	5665.62	5665.4530	0.167
(7 7)	5041.65	5041.8052	-0.155
(9 7)	6385.04	6384.7165	0.324
(8 8)	5773.90	5774.0965	-0.196
(9 9)	6509.47	6509.6415	-0.171

<sup>a</sup> Cylindrical oscillator basis quantum labels assigned to the optimized eigenvectors.

<sup>b</sup> Experimental energies from Ref. [89].

<sup>c</sup> Calculated energies.

<sup>d</sup> Difference between experimental and calculated energies.

### 3.1.3. Hydrogen Isocyanide, HNC

Hydrogen isocyanide is an isotopomer of hydrogen cyanide with only 19 experimental energy levels published in the literature [91; 92]. We have obtained a sizable improvement in the fit to this molecule with respect to the results published in Ref. [51]; managing to get a decrease in the *rms* from  $2.3 \text{ cm}^{-1}$  to  $0.08 \text{ cm}^{-1}$  with the addition of only one extra interaction: the 3-body term  $\hat{n}\hat{\ell}^2$ .



The experimental and calculated vibrational energies are reported in Tab. 4. All the states are well below the isomerization transition state energy, which lies around  $12,000 \text{ cm}^{-1}$  [54].

The calculated energies and eigenstates for the optimized Hamiltonian have been used in preparing the figures in the different panels of Fig. 4. One should emphasize that the quantum monodromy plot (upper left panel) seems to indicate a linear equilibrium geometrical configuration for this molecule, something that is confirmed from the energy functional (lower right panel), where we made use of the bond equilibrium lengths from [90].

However, the Birge-Sponer diagram (upper right panel of Fig. 4) is more complex than expected for a linear molecule, with noticeably different behavior for states with different vibrational angular momentum values. Besides, the participation ratio diagram (lower left panel of Fig. 4) shows, for  $\ell = 0$  states, a crossing around  $3,000 \text{ cm}^{-1}$  after which states are better localized in the  $SO(3)$  basis set than in the  $U(2)$  basis set. As already highlighted in Ref. [51], the Birge-Sponer plot indicates that there is a competition between anharmonicity and pairing operators in the subspaces with different vibrational angular momenta. The inclusion of the new cubic term seems to conveniently tackle with this. In any case, the eigenvectors are more complex than for a simple linear molecule, as can be deduced from the crossing of the two curves of the PR plot. This may be due to the proximity to the isomerization barrier in this system which lies around  $12,000 \text{ cm}^{-1}$ , but it seems too far to explain such a low energy feature in the PR [54].



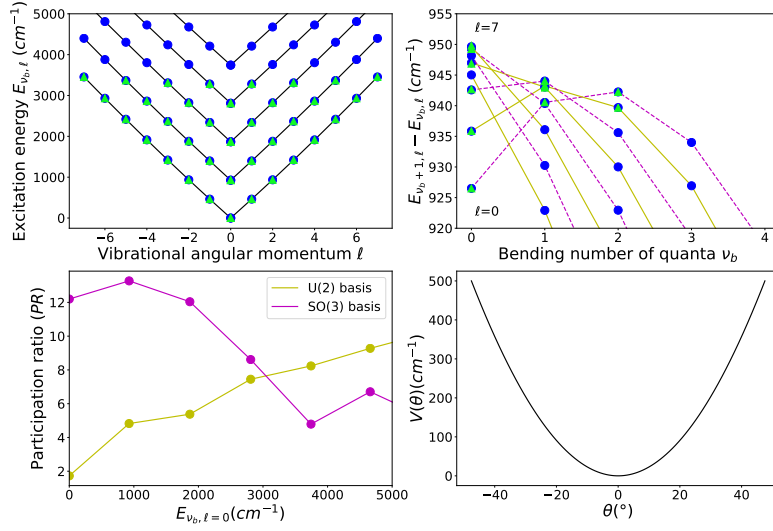


Figure Fig. 4: The upper row shows the quantum monodromy plot (upper left panel) and the Birge-Sponer plot (upper right panel) for the bending mode of HNC with blue circles (green triangles) for calculated (experimental) data. The lower row includes the PR for  $\ell = 0$  eigenstates in the two bases considered as a function of the state energy (lower left panel) and the bending energy functional derived using the coherent state formalism (lower right panel).



Table Tab. 4: Experimental and calculated term values and residuals for the bending mode of HNC. Units of  $\text{cm}^{-1}$ .

$(n, \ell)^a$	Exp. <sup>b</sup>	Cal. <sup>c</sup>	Exp.-Cal. <sup>d</sup>
( 2 0)	926.50	926.5071	-0.007
( 4 0)	1867.05	1867.0497	0.000
( 6 0)	2809.29	2809.2992	-0.009
( 1 1)	462.72	462.6863	0.034
( 3 1)	1398.56	1398.5296	0.030
( 5 1)	2341.84	2341.7558	0.084
( 7 1)	3281.50	3281.4508	0.049
( 2 2)	936.05	936.1066	-0.057
( 4 2)	1878.72	1878.6866	0.033
( 6 2)	2822.75	2822.7088	0.041
( 3 3)	1419.97	1419.9198	0.050
( 5 3)	2366.83	2366.9073	-0.077
( 7 3)	3309.78	3309.9472	-0.167
( 4 4)	1913.87	1913.8403	0.030
( 6 4)	2863.11	2863.1206	-0.011
( 5 5)	2417.57	2417.6251	-0.055
( 7 5)	3367.37	3367.2552	0.115
( 6 6)	2930.90	2931.0649	-0.165
( 7 7)	3453.78	3453.9760	-0.196

<sup>a</sup> Cylindrical oscillator basis quantum labels assigned to the optimized eigenvectors.

<sup>b</sup> Experimental energies from Ref. [91; 92].

<sup>c</sup> Calculated energies.

<sup>d</sup> Difference between experimental and calculated energies.

#### 3.1.4. Cyanofulminate, *NCCNO*

The experimental data of the CCN bending mode  $\nu_7$  –linear molecule notation– of cyanofulminate have been recorded and analyzed using a semirigid bender effective Hamiltonian [93]. We have made a fit to the eleven available experimental data for this bending degree of freedom with the Hamiltonian in Eq. 10. In this case, one-body and two-body interactions are enough to get a fit with an  $rms=0.27 \text{ cm}^{-1}$  ( $\sigma = 0.22 \text{ cm}^{-1}$ ), whereas the semirigid bender model obtained a standard deviation  $\sigma = 0.66 \text{ cm}^{-1}$  [93]. The calculated energies are compared in Tab. 5 with the experimental data. In addition, to compare the predictive power of our results versus an alternative approach, we also include the computed semirigid bender energies in some cases when experimental values are not available. In general, there is less than 1% energy difference between the results of the semirigid bender model and those from this work. In Ref. [50] the one- and two-body algebraic Hamiltonian was fitted to the calculated semirigid bender energies, obtaining an  $rms$  of  $0.16 \text{ cm}^{-1}$ . In the present work, with the same number of parameters than [50] and fitting to the available experimental dataset, we have obtained an  $rms = 0.09 \text{ cm}^{-1}$ .

Using the optimized energy term values and eigenstates, the different pan-



els of Fig. 5 have been plotted. The quantum monodromy plot (upper left panel) indicates that this is a linear molecule, something confirmed by the energy functional (lower right panel) well-defined minimum at zero. The necessary information on the geometric structure of the molecule to scale the energy functional has been taken from [93]. However, and in the same way as it happens with HNC, the Birge-Sponer diagram (upper right panel) evinces a strong dependence on vibrational angular momentum and the switch, in some cases, from positive to negative anharmonicity. The PR plot (lower left panel), in the same way as happened for HNC, shows a crossing of the lines associated to the two bases in the cyanofulminate case.

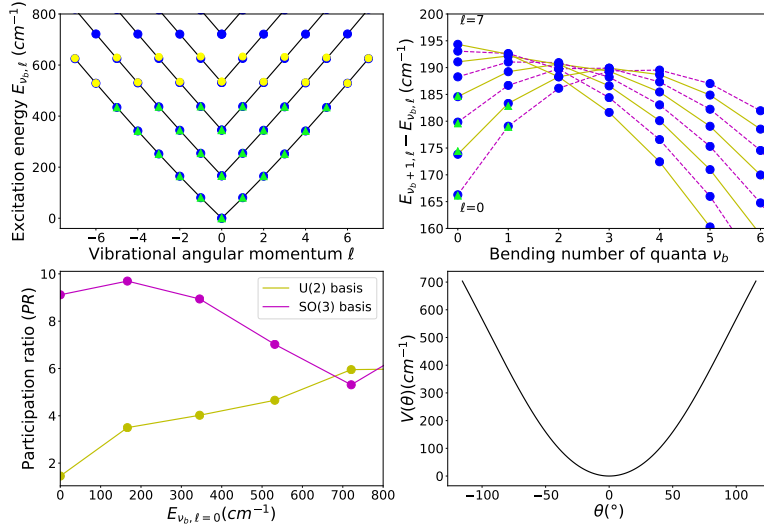


Figure Fig. 5: The upper row shows the quantum monodromy plot (upper left panel) and the Birge-Sponer plot (upper right panel) for the  $\nu_7$  bending mode of NCCNO with blue circles (green triangles) for calculated (experimental) data, and yellow circles for the results of the semirigid bender model [93]. The lower row includes the PR for  $l = 0$  eigenstates in the two bases considered as a function of the state energy (lower left panel) and the bending energy functional derived using the coherent state formalism (lower right panel).



Table Tab. 5: Experimental and calculated term values and residuals for the  $\nu_7$  bending mode of cyanofulminate. Units of  $\text{cm}^{-1}$ .

$(n, \ell)^a$	Exp. <sup>b</sup>	Cal. <sup>c</sup>	Exp.-Cal. <sup>d</sup>
(2 0)	166.1183	166.2766	-0.158
(4 0)	345.0648	345.3459	-0.281
(6 0)	535.45 <sup>e</sup>	531.4906	3.959
(1 1)	80.5242	80.4896	0.035
(3 1)	254.9342	254.3217	0.613
(5 1)	437.7442	437.6471	0.097
(7 1)	633.43 <sup>e</sup>	625.9407	7.489
(2 2)	164.6042	164.6148	-0.011
(4 2)	344.1999	344.4462	-0.246
(6 2)	534.69 <sup>e</sup>	531.1341	3.556
(3 3)	251.8017	251.8713	-0.070
(5 3)	436.5020	436.4496	0.052
(7 3)	632.17 <sup>e</sup>	625.6879	6.482
(4 4)	341.7811	341.8514	-0.070
(6 4)	532.48 <sup>e</sup>	530.1291	2.351
(5 5)	434.2764	434.2129	0.063
(7 5)	629.71 <sup>e</sup>	625.2862	4.424
(6 6)	528.92 <sup>e</sup>	528.6598	0.260
(7 7)	626.60 <sup>e</sup>	624.9297	1.670

<sup>a</sup> Cylindrical oscillator basis quantum labels assigned to the optimized eigenvectors.

<sup>b</sup> Experimental energies from Ref. [93].

<sup>c</sup> Calculated energies.

<sup>d</sup> Difference between experimental and calculated energies.

<sup>e</sup> Computed energies using the semirigid bender model [93]. They have not been used as an input in the fit but they are included to compare the present work with the results of a different approach.

### 3.2. Bent Molecules

In this subsection we address the modeling of the  $\nu_2$  bending mode for four triatomic bent molecules: hydrogen sulfide ( $\text{H}_2\text{S}$ ), hydrogen selenide ( $\text{H}_2\text{Se}$ ), silylene ( $\text{SiH}_2$ ), and ozone ( $\text{O}_3$ ). All of them can be characterized using the interactions associated with the displaced oscillator chain in the four-body Hamiltonian of the 2DVM, except ozone, that requires a six-body term,  $\hat{\ell}^4\hat{W}^2$ , but still in the same  $SO(3)$  dynamical symmetry. Therefore, the Hamiltonian for these species,  $\hat{H}_{bent}$ , is diagonal in the displaced oscillator chain basis (Eq. 4)

$$\hat{H}_{bent} = P_{22}\hat{\ell}^2 + P_{23}\hat{W}^2 + P_{43}\hat{\ell}^4 + P_{44}\hat{\ell}^2\hat{W}^2 + P_{46}\hat{W}^4 + P_6\hat{\ell}^4\hat{W}^2 + B|\hat{\ell}| + B_{\nu_b}\hat{W}^2|\hat{\ell}|, \quad (\text{Eq. 17})$$

and no interaction involving the number operator  $\hat{n}$  is included in the analysis.

Furthermore, taking into consideration that the four molecules under study,  $\text{H}_2\text{S}$ ,  $\text{H}_2\text{Se}$ ,  $\text{SiH}_2$ , and  $\text{O}_3$ , are asymmetric-top molecules, we have also added to the Hamiltonian (Eq. 17) operators that are linear in the absolute value of



the vibrational angular momentum,  $|\ell|$ , to improve the fit of the rovibrational energy levels  $|\nu_b; J, K_a = J, K_c = 0\rangle$ . The quantum numbers  $K_a$  and  $K_c$  are the projections in the molecular fixed frame system of the rotational angular momentum  $J$  along the  $z$ -axis and  $y$ -axis, respectively (assuming the  $I^r$  convention). The need of these extra interaction terms and the parameters  $B$  and  $B_{\nu_b}$  in Eq. 17 can be explained by the linear  $J$  term that stems from the rotational term  $J(J+1)$  in the rovibrational Hamiltonian (see for example [94; 95]). The parameter  $B_{\nu_b}$  introduces a centrifugal correction.

The optimized Hamiltonian (Eq. 17) spectroscopic parameters are given in Tab. 6, where we also include the number of experimental energy terms included in the fit, the total number of vibrons ( $N$ ), the present study  $rms$  ( $rms_n$ ) and, when available, for the sake of comparison, the  $rms$  obtained in [51] ( $rms_o$ ). The noticeable enhancement of the  $H_2S$  and  $H_2Se$  fits, lowering down the  $rms$  close to experimental accuracy, is basically due to the inclusion of the linear  $|\ell|$  interaction term with the  $B$  spectroscopic parameter.

In this case, as well as in the nonrigid molecules case, we have directly connected the  $r$  intrinsic approach classical variable to the deviation of linearity angle,  $\theta(rad) = \frac{\theta_e(rad)}{r_{min}}r$ , making use of the experimental information on the molecular equilibrium structure. In this way the plot has the energy functional minimum located at the right position though we are not truly predicting this structure. We are planning to develop a more involved scaling in a future work. The experimental equilibrium angle values are given in Tab. 6.



Table Tab. 6: Optimized Hamiltonian parameters (in  $\text{cm}^{-1}$  units) for the bent molecules considered. Values are given with their associated uncertainty in parentheses in units of the last quoted digits. The total vibron number and the  $rms$  obtained in this work,  $rms_n$ , are also included. For the sake of comparison, the  $rms$  obtained in Ref. [51], if available, is also shown, labeled as  $rms_o$ .

	H <sub>2</sub> S	H <sub>2</sub> Se	SiH <sub>2</sub>	O <sub>3</sub>
$P_{22}$	19.29(25)	18.27(10)	17.2(3)	7.72(3)
$P_{23}$	-2.489(9)	-1.81(15)	-1.81593(10)	-0.7226(21)
$P_{43}$	-1.48(5)e-3	1.17(10)e-3	-	-1.722(6)e-3
$P_{44}$	-4.56(13)e-4	-3.49(3)e-4	-4.85(16)e-04	-4.63(3)e-5
$P_{46}$	9.51(25)e-6	5.1(3)e-6	-	7.67(12)e-7
$P_6$	-	-	-	1.72(6)e-8
$B$	39.2(3)	7.44(17)	7.01(7)	0.553(16)
$B_{\nu_b}$	-1.58(14)e-3	-	-	-
N	140	170	138	300
$rms_n$	1.09	0.87	0.18	0.17
$rms_o$	5.9 <sup>a</sup>	5.9 <sup>a</sup>	-	-
$N_{data}$	57	46	12	51
$\theta_e$	92.23 <sup>o b</sup>	89.43 <sup>o c</sup>	87.73 <sup>o d</sup>	63.25 <sup>o e</sup>

<sup>a</sup> The results obtained in this work are presented with the ones obtained in a previous work in spite of the number of data considered for H<sub>2</sub>S and H<sub>2</sub>Se were 35 and 45, respectively [51].

<sup>b</sup> The equilibrium deviation to linearity angle for H<sub>2</sub>S has been taken from Ref. [96].

<sup>c</sup> The equilibrium deviation to linearity angle for H<sub>2</sub>Se has been taken from Ref. [97].

<sup>d</sup> The equilibrium deviation to linearity angle for SiH<sub>2</sub> has been taken from Ref. [98].

<sup>e</sup> The equilibrium deviation to linearity angle for O<sub>3</sub> has been extracted from Ref. [99].

### 3.2.1. Hydrogen Sulfide, H<sub>2</sub>S

The rovibrational spectrum of hydrogen sulfide has been exhaustively studied (see, e.g., the references in [95]). Nevertheless, the rovibrational energies for the bending overtones are only known in bands up to  $\nu_2 = 5$  inclusive. However the  $\nu_2 = 4$  level information reported in the literature is exclusively its vibrational energy [100; 101; 102; 103; 104]. The 2DVM four-body Hamiltonian (Eq. 17) has been used to analyze the 57 available experimental bending rovibrational levels  $|\nu_b; J, K_a = J, K_c = 0\rangle$  up to  $J = K_a = 17$ . The analysis started with the fit of the first five parameters of Eq. 17, obtaining an  $rms$  of  $9.56 \text{ cm}^{-1}$ . Once the parameter  $B$  is included, the  $rms$  decreases to  $2.02 \text{ cm}^{-1}$ . The final results, including the seven parameters of Eq. 17, have an  $rms$  of  $1.09 \text{ cm}^{-1}$ . The calculated energies, shown in Tab. 7, agree well with the experimental spectrum. This agreement is sensitively better than the agreement obtained in Ref. [51], where only 35 experimental term values were included in the fit. Therefore, the present four-body Hamiltonian plus the rotational energy correction achieves a significant improvement in the optimization. In Ref. [51] an  $rms$  of  $5.9 \text{ cm}^{-1}$  was obtained, whereas the same Hamiltonian plus the extra parameter  $B$  (Eq. 17), associated to the linear term of the matrix element of  $\hat{J}^2$ , decreases the  $rms$  to  $0.6 \text{ cm}^{-1}$ .

The optimized energy term values and eigenvectors obtained from the Hamil-



tonian parameters (Eq. 17) have been used to compute the quantities depicted in the different panels of Fig. 6. The quantum monodromy plot and Birge-Sponer diagram obtained in this case have the expected signatures associated with semirigid bent molecules. The PR, depicted in the bottom left panel shows, as trivially expected from the optimization procedure, that the  $SO(3)$  displaced oscillator basis set is the best option to characterize this molecule.

The energy functional for the system is depicted in the lower right panel of Fig. 6, and it is computed from the optimized Hamiltonian parameters. We only depict this functional up to a maximum energy of 12,000  $\text{cm}^{-1}$  because the lack of data for highly-excited states results in an unphysical estimate of the potential barrier to linearity. This is due to the low energy of the available experimental term values. Being so close to the bottom of the potential energy surface, they fail to provide enough information to the model to correctly reproduce the barrier to linearity barrier; in fact the obtained value is larger than 40,000  $\text{cm}^{-1}$  and very similar to the result obtained in Ref. [51]. However, if the input includes energy levels closer to the barrier, the results would significantly improve, providing a much better estimate to the barrier to linearity, i.e. the critical energy of the ESQPT. In a different context (isomerization reactions) a similar situation has been recently tackled with by the authors [54].

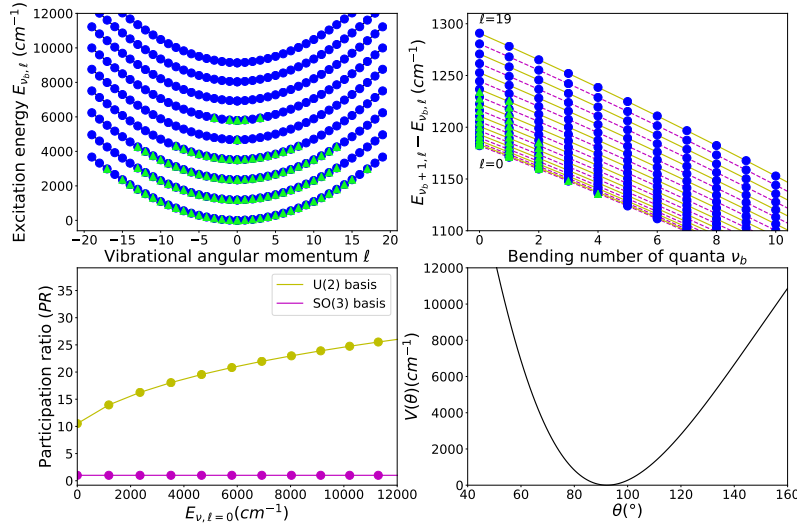


Figure Fig. 6: The upper row shows the quantum monodromy plot (upper left panel) and the Birge-Sponer plot (upper right panel) for  $\text{H}_2\text{S}$  bending mode, using blue circles (green triangles) for calculated (experimental) data. The lower row includes the PR for  $l = 0$  eigenstates in the two bases considered as a function of the state energy (lower left panel) and the bending energy functional derived using the coherent state formalism (lower right panel).



Table Tab. 7: Experimental and calculated term values and residuals for the bending mode of hydrogen sulfide with quantum numbers  $(\nu_b, J, K_a = J)$  ( $A_1$  or  $B_2$  symmetry). Units of  $\text{cm}^{-1}$ .

$(\nu_b, K_a)^a$	Exp. <sup>b</sup>	Cal. <sup>c</sup>	Exp.-Cal. <sup>d</sup>	$(\nu_b, K_a)^a$	Exp. <sup>b</sup>	Cal. <sup>c</sup>	Exp.-Cal. <sup>d</sup>
(0 0)	0.00	0.0000	0.000	(1 12)	2774.58	2776.0501	-1.470
(0 1)	19.38	18.3657	1.014	(1 13)	3034.27	3036.7975	-2.527
(0 2)	58.37	57.2700	1.100	(2 0)	2353.96	2353.1907	0.769
(0 3)	117.39	116.6595	0.730	(2 1)	2374.52	2373.8105	0.709
(0 4)	196.80	196.4455	0.354	(2 2)	2415.95	2415.9804	-0.030
(0 5)	296.68	296.5037	0.176	(2 3)	2478.79	2479.6471	-0.857
(0 6)	416.85	416.6742	0.176	(2 4)	2563.44	2564.7219	-1.282
(0 7)	557.03	556.7618	0.268	(2 5)	2669.91	2671.0804	-1.170
(0 8)	716.92	716.5355	0.384	(2 6)	2797.91	2798.5629	-0.653
(0 9)	896.20	895.7290	0.471	(2 7)	2947.02	2946.9740	0.046
(0 10)	1094.52	1094.0405	0.479	(2 8)	3116.81	3116.0828	0.727
(0 11)	1311.55	1311.1326	0.417	(2 9)	3306.83	3305.6231	1.207
(0 12)	1546.92	1546.6323	0.288	(2 10)	3516.62	3515.2928	1.327
(0 13)	1800.25	1800.1312	0.119	(2 11)	3745.70	3744.7547	0.945
(0 14)	2071.18	2071.1854	-0.005	(2 12)	3993.58	3993.6358	-0.056
(0 15)	2359.33	2359.3154	0.015	(2 13)	4259.78	4261.5278	-1.748
(0 17)	2985.78	2984.7077	1.072	(3 0)	3513.79	3512.8029	0.987
(1 0)	1182.58	1182.1728	0.407	(3 1)	3535.01	3534.5253	0.485
(1 1)	1202.52	1201.6736	0.846	(3 2)	3577.82	3578.2926	-0.473
(1 2)	1242.69	1242.2225	0.467	(3 3)	3642.81	3644.0516	-1.242
(1 3)	1303.54	1303.7661	-0.226	(3 4)	3730.40	3731.7135	-1.314
(1 4)	1385.47	1386.2156	-0.746	(3 5)	3840.55	3841.1540	-0.604
(1 5)	1488.53	1489.4467	-0.917	(3 6)	3972.88	3972.2133	0.667
(1 6)	1612.48	1613.2996	-0.820	(3 7)	4126.90	4124.6960	2.204
(1 7)	1756.98	1757.5789	-0.599	(3 8)	4302.09	4298.3713	3.719
(1 8)	1921.68	1922.0539	-0.374	(4 0)	4661.68	4660.7620	0.918
(1 9)	2106.19	2106.4582	-0.268	(5 0)	5797.24	5796.8242	0.416
(1 10)	2310.12	2310.4898	-0.370	(5 1)	5819.97	5820.7030	-0.733
(1 11)	2533.05	2533.8114	-0.761	(5 3)	5935.82	5937.4454	-1.625

<sup>a</sup> Displaced oscillator basis quantum labels assigned to the optimized eigenvectors.

<sup>b</sup> Experimental energies from [100; 101; 102; 103; 104].

<sup>c</sup> Calculated energies.

<sup>d</sup> Difference between experimental and calculated energies.

### 3.2.2. Hydrogen Selenide, $H_2^{80}\text{Se}$

Several comprehensive theoretical analyses of the infrared spectrum of the main isotopologue of hydrogen selenide can be found in the literature (see, *e.g.*, [94; 97; 105; 106; 107]). The present work analysis is only focused on the bending degree of freedom, and we take into consideration all the available experimental bending rovibrational levels (up to  $\nu_2 = 3$  and  $J = 13$ , inclusive) [105; 108; 109; 110; 111; 112]. The six-parameters in the Hamiltonian of Eq. 17 are fitted to



the  $|\nu_b; J, K_a = J, K_c = 0\rangle$  experimental levels (46 experimental data) obtaining an  $rms = 0.87 \text{ cm}^{-1}$ . The very good agreement between experimental and calculated levels can be appreciated in Tab. 8. The obtained results significantly improve the results obtained for this molecular species in Ref. [51], where only 45 experimental term values were considered. The present study achieves an  $rms$  of  $0.87 \text{ cm}^{-1}$  (for 46 experimental data) compared to  $5.9 \text{ cm}^{-1}$  in [51]. The main culprit for this improvement is the inclusion of the  $B$  parameter in (Eq. 17).

The different quantities depicted in Fig. 7 illustrate that, as expected, the hydrogen selenide bending degree of freedom classical limit is akin to the hydrogen sulfide one (see Subsect. 3.2.1), sharing spectroscopic signatures typical of semirigid bent molecules. For the same reasons than in the  $\text{H}_2\text{S}$  case, the energy functional in the lower right panel has been plotted up to a maximum energy of  $10,000 \text{ cm}^{-1}$ , due to the unphysical value of the predicted barrier to linearity.

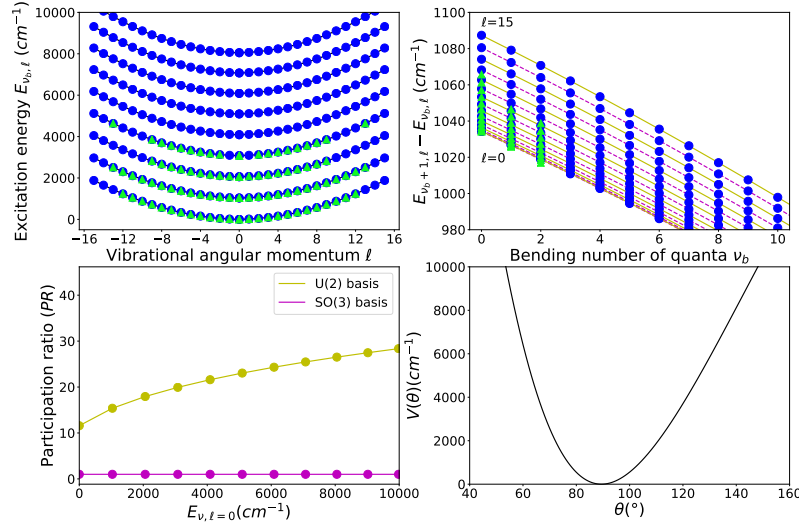


Figure Fig. 7: The upper row shows the quantum monodromy plot (upper left panel) and the Birge-Sponer plot (upper right panel) for the bending mode of  $\text{H}_2\text{Se}$ , using blue circles (green triangles) for calculated (experimental) data. The lower row includes the PR for  $\ell = 0$  eigenstates in the two bases considered as a function of the state energy (lower left panel) and the bending energy functional derived using the coherent state formalism (lower right panel).



Table Tab. 8: Experimental and calculated term values and residuals for the bending mode of hydrogen selenide with quantum numbers  $(\nu_b, J, K_a = J)$  ( $A_1$  or  $B_2$  symmetry). Units of  $\text{cm}^{-1}$ .

$(\nu_b, K_a)^a$	Exp. <sup>b</sup>	Cal. <sup>c</sup>	Exp.-Cal. <sup>d</sup>	$(\nu_b, K_a)^a$	Exp. <sup>b</sup>	Cal. <sup>c</sup>	Exp.-Cal. <sup>d</sup>
(0 1)	15.87	15.5685	0.301	(1 11)	2110.45	2111.0362	-0.586
(0 2)	47.65	47.3775	0.272	(1 12)	2303.40	2303.7411	-0.341
(0 3)	95.38	95.3849	-0.005	(1 13)	2511.24	2511.1524	0.088
(0 4)	159.09	159.5205	-0.431	(2 0)	2059.97	2060.7033	-0.733
(0 5)	238.86	239.6861	-0.826	(2 1)	2076.75	2076.7419	0.008
(0 6)	334.64	335.7553	-1.115	(2 2)	2110.33	2109.9614	0.369
(0 7)	446.35	447.5737	-1.224	(2 3)	2160.80	2160.3195	0.481
(0 8)	573.90	574.9589	-1.059	(2 4)	2228.18	2227.7461	0.434
(0 9)	717.10	717.7004	-0.600	(2 5)	2312.49	2312.1429	0.347
(0 10)	875.60	875.5595	0.041	(2 6)	2413.69	2413.3837	0.306
(0 11)	1049.20	1048.2695	0.931	(2 7)	2531.60	2531.3139	0.286
(0 12)	1237.70	1235.5357	2.164	(2 8)	2666.03	2665.7513	0.279
(1 0)	1034.17	1034.1543	0.016	(2 9)	2816.70	2816.4851	0.215
(1 1)	1050.50	1049.9593	0.541	(3 0)	3076.92	3079.4832	-2.563
(1 2)	1083.17	1082.4777	0.692	(3 2)	3128.77	3129.6649	-0.895
(1 3)	1132.23	1131.6674	0.563	(3 3)	3180.73	3181.1774	-0.447
(1 4)	1197.72	1197.4583	0.262	(3 4)	3250.11	3250.2202	-0.110
(1 5)	1279.68	1279.7520	-0.072	(3 5)	3336.93	3336.6950	0.235
(1 6)	1378.06	1378.4224	-0.362	(3 6)	3441.10	3440.4755	0.625
(1 7)	1492.75	1493.3149	-0.565	(3 7)	3562.43	3561.4073	1.023
(1 8)	1623.56	1624.2471	-0.687	(3 8)	3700.64	3699.3079	1.332
(1 9)	1770.28	1771.0084	-0.728	(3 9)	3855.44	3853.9668	1.473
(1 10)	1932.66	1933.3604	-0.700	(3 13)	4633.70	4634.9922	-1.292

<sup>a</sup> Displaced oscillator basis quantum labels assigned to the optimized eigenvectors.

<sup>b</sup> Experimental energies from Refs. [105; 108; 109; 110; 111; 112].

<sup>c</sup> Calculated energies.

<sup>d</sup> Difference between experimental and calculated energies.

### 3.2.3. Silylene, $\text{SiH}_2$

The rovibrational structure of several electronic states of silylene has been the subject of both theoretical and experimental works (see, e.g., [113; 114; 115; 116; 117]). Nevertheless, the ground electronic state rovibrational spectrum is still not completely resolved experimentally. In fact, the scarcity of experimental data has been recently circumvented with a comprehensive variational calculation, obtaining a molecular line list which has allowed for the analysis and assignment of the current measurements [118].

As in the previous cases, we introduce in our analysis the rotational energies with  $K_a = J$  and  $K_c = 0$ , in this case up to  $J = K_a = 5$ , of the excited bending  $\nu_2$  bands. There are 12 experimental bending term values available, the highest bending overtone recorded is  $\nu_b = 3$ , and most experimental data stems from [114; 115], though some rotational energy levels of the  $\nu_2$  band have



been computed by [118] with the spectroscopic constants from [114]. The experimental energies from [113] have not been included because they are displaced around  $3.5 \text{ cm}^{-1}$  [118].

We have obtained a good agreement with the experiment considering exclusively operators associated with the displaced oscillator dynamical symmetry, as in the previously modeled bent molecules. The *rms* of the four parameter fit is equal to  $0.18 \text{ cm}^{-1}$  (see Tab. 6 and Tab. 9). This Hamiltonian has been used to predict higher bending overtones and, with the resulting eigenvalues and eigenstates, Fig. 8 has been depicted. It should be highlighted that we have not included in our fit the experimental  $2\nu_2$  and  $4\nu_2$  bands [115]. These levels have also been excluded from the calculations in [118] due to possible misassignments or perturbations by resonances with stretching degrees of freedom, in particular Fermi resonances [115]. Nevertheless, their energy term values have been predicted (see Supplementary Material) with residuals around  $5 \text{ cm}^{-1}$  for  $2\nu_2$  and several tens of wave numbers for  $4\nu_2$ , respectively.

The upper two panels in Fig. 8, the quantum monodromy diagram (left) and the Birge-Sponer plot (right) indicate that the silylene molecule is an archetypal bent molecule, such as hydrogen sulfide and hydrogen selenide, up to the maximum energies depicted in the figure, including the fifth excited bending state. The dependence of the energy on the angular momentum is roughly quadratic in the quantum monodromy diagram and anharmonicities are negative in the Birge-Sponer plot. The PR plot, in the lower left panel, shows a regular increase of delocalization in the cylindrical oscillator (linear) basis up to rather high energy values, confirming the bent character of silylene. We also provide the bending energy functional for this molecule in the lower right panel.



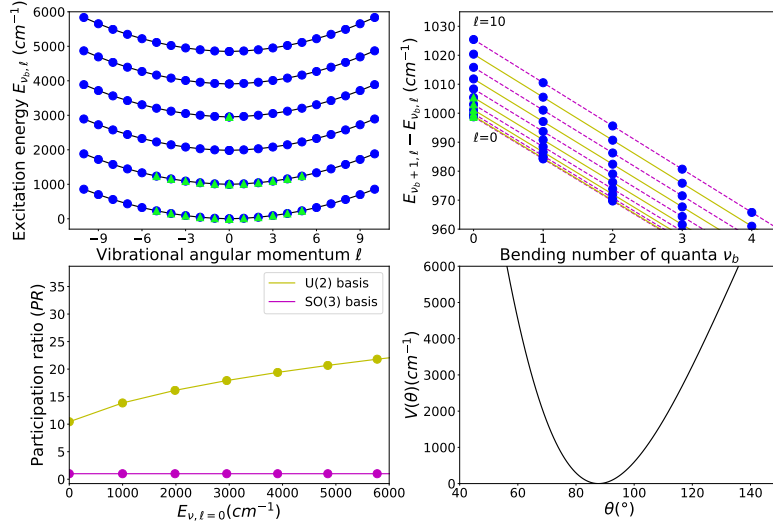


Figure Fig. 8: The upper row shows the quantum monodromy plot (upper left panel) and the Birge-Sponer plot (upper right panel) for the bending mode of silylene, using blue circles (green triangles) for calculated (experimental) data. The lower row includes the PR for  $\ell = 0$  eigenstates in the two bases considered as a function of the state energy (lower left panel) and the bending energy functional derived using the coherent state formalism (lower right panel).



Table Tab. 9: Experimental and calculated term values and residuals for the bending mode of silylene with quantum numbers  $(\nu_b, J, K_a = J)$  ( $A_1$  or  $B_2$  symmetry). Units of  $\text{cm}^{-1}$ .

$(\nu_b, K_a)^a$	Exp. <sup>b</sup>	Calc. <sup>c</sup>	Exp.-Calc. <sup>d</sup>
(0 1)	15.12	14.8772	0.243
(0 2)	45.56	45.4874	0.077
(0 3)	91.68	91.8305	-0.155
(0 4)	153.75	153.9065	-0.157
(0 5)	231.85	231.7154	0.138
(1 0)	998.62	998.7641	-0.140
(1 1)	1014.14	1013.9081	0.233
(1 2)	1045.42	1045.3184	0.100
(1 3)	1092.86	1092.9952	-0.134
(1 4)	1156.79	1156.9384	-0.144
(1 5)	1237.27	1237.1480	0.118
(3 0)	2952.7 <sup>e</sup>	2952.7098	-0.010

<sup>a</sup> Displaced oscillator basis quantum labels assigned to the optimized eigenvectors.

<sup>b</sup> Experimental energies from Refs. [114; 115].

<sup>c</sup> Calculated energies.

<sup>d</sup> Difference between experimental and calculated energies.

<sup>e</sup> Experimental energies with a large discrepancy relative to the data computed by [118].

### 3.2.4. Ozone, $O_3$

Ozone, with a  $C_{2v}(M)$  molecular symmetry, is a molecule of a significant relevance in different fields: atmospheric and pollution studies, astrochemistry, climatology, for industrial applications, etc. This has fostered an exhaustive spectroscopic study of the ozone molecule along the last years (see, e.g., [119; 120; 121; 122; 123; 124; 125; 126]). Concerning the pure bending band, the available experimental data include levels up to  $\nu_b = 4$  and up to angular momentum  $J = 28$  [119; 121; 122; 123; 124]. The 51 experimental rovibrational energy levels considered in this work have been obtained from the analysis of effective Hamiltonians in a polyad scheme [125].

We have performed a first fit, obtaining an *rms* of  $0.74 \text{ cm}^{-1}$ , varying six parameters from Hamiltonian (Eq. 17): the five 4-body interaction parameters plus  $B$ . In a second, and final fit, we have included an extra 6-body interaction ( $\hat{\ell}^4 \hat{W}^2$ ) in the Hamiltonian (Eq. 17), managing to diminish the *rms* to  $0.17 \text{ cm}^{-1}$  (Tab. 6). Hence, experimental data have been reproduced within experimental accuracy with a Hamiltonian with seven adjustable interaction terms (see Tab. 10). Such a good agreement can be explained considering that the bending states in this molecule are hardly affected by the resonances defining the polyad structure of the rovibrational spectrum of ozone [125].

We have used the energies and eigenstates predicted by the optimized Hamiltonian to depict the different quantities included in Fig. 9. From these plots it can be deduced that ozone has, as expected, the typical spectroscopic signatures of a bent molecular system, as the rest of the examples considered in the present subsection. No hint of spectroscopic signatures associated with a linear config-



uration can be found. The dependence of energy as a function of vibrational angular momentum is quadratic in the quantum monodromy diagram and the anharmonicity is negative for all bending overtone series in the Birge-Sponer plot. As expected, the PR is minimal for the displaced oscillator basis set and there is a smooth decrease of localization in the cylindrical oscillator basis. The bending energy functional around the equilibrium configuration is also provided.

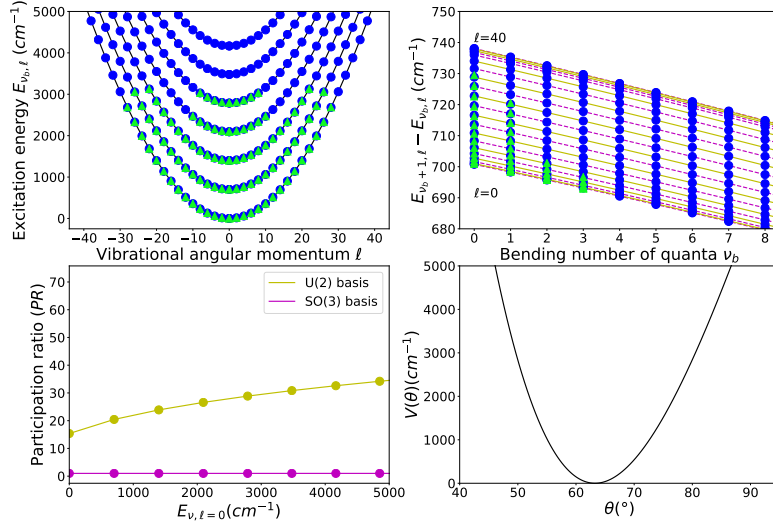


Figure Fig. 9: The upper row shows the quantum monodromy plot (upper left panel) and the Birge-Sponer plot (upper right panel) for the bending mode of ozone, using blue circles (green triangles) for calculated (experimental) data. The lower row includes the PR for  $\ell = 0$  eigenstates in the two bases considered as a function of the state energy (lower left panel) and the bending energy functional derived using the coherent state formalism (lower right panel).



Table Tab. 10: Experimental and calculated term values and residuals for the bending mode of ozone with quantum numbers  $(\nu_b, J, K_a = J)$  ( $A_1$  or  $B_2$  symmetry). Units of  $\text{cm}^{-1}$ .

$(\nu_b, K_a)^a$	Exp. <sup>b</sup>	Cal. <sup>c</sup>	Exp.-Cal. <sup>d</sup>	$(\nu_b, K_a)^a$	Exp. <sup>b</sup>	Cal. <sup>c</sup>	Exp.-Cal. <sup>d</sup>
(0 0)	0.00	0.0000	0.00000	(1 22)	2406.35	2406.6551	-0.30746
(0 2)	15.05	15.2486	-0.19667	(1 24)	2719.44	2719.6056	-0.16821
(0 4)	58.49	58.7486	-0.26302	(1 26)	3056.39	3056.0136	0.37360
(0 6)	130.18	130.4020	-0.21982	(2 0)	1399.27	1399.0529	0.22008
(0 8)	229.94	230.0456	-0.10109	(2 2)	1414.75	1414.7431	0.00881
(0 10)	357.50	357.4508	0.05172	(2 4)	1459.47	1459.5599	-0.08728
(0 12)	512.52	512.3241	0.19464	(2 6)	1533.29	1533.3818	-0.09048
(0 14)	694.59	694.3062	0.28743	(2 8)	1635.97	1636.0061	-0.03571
(0 16)	903.27	902.9728	0.30035	(2 10)	1767.19	1767.1492	0.03725
(0 18)	1138.06	1137.8343	0.22141	(2 12)	1926.54	1926.4464	0.09104
(0 20)	1398.40	1398.3357	0.06375	(2 14)	2113.55	2113.4519	0.09938
(0 22)	1683.73	1683.8570	-0.12673	(2 16)	2327.69	2327.6391	0.05579
(0 24)	1993.45	1993.7125	-0.26303	(2 18)	2568.38	2568.4000	-0.01835
(0 26)	2326.94	2327.1515	-0.20735	(2 20)	2834.98	2835.0459	-0.06708
(0 28)	2683.60	2683.3580	0.24131	(2 22)	3126.81	3126.8068	0.00491
(1 0)	700.93	700.7761	0.15489	(3 0)	2094.99	2094.7866	0.20540
(1 2)	716.19	716.2463	-0.05345	(3 2)	2110.69	2110.6954	-0.00337
(1 4)	760.26	760.4069	-0.14792	(3 4)	2156.09	2156.1640	-0.07461
(1 6)	833.00	833.1481	-0.14925	(3 6)	2231.02	2231.0592	-0.03694
(1 8)	934.20	934.2870	-0.09084	(3 8)	2335.23	2335.1589	0.07096
(1 10)	1063.56	1063.5675	-0.01202	(3 10)	2468.36	2468.1521	0.20570
(1 12)	1220.71	1220.6601	0.04800	(4 0)	2787.90	2787.9336	-0.03362
(1 14)	1405.22	1405.1624	0.05762	(4 2)	2803.89	2804.0595	-0.17055
(1 16)	1616.60	1616.5985	0.00104	(4 4)	2850.00	2850.1755	-0.17546
(1 18)	1854.31	1854.4196	-0.11330	(4 6)	2926.10	2926.1368	-0.03599
(1 20)	2117.76	2118.0035	-0.24397	(4 8)	3031.90	3031.7018	0.19390

<sup>a</sup> Displaced oscillator basis quantum labels assigned to the optimized eigenvectors.

<sup>b</sup> Experimental energies from Refs. [119; 121; 122; 123; 124; 125].

<sup>c</sup> Calculated energies.

<sup>d</sup> Differences between experimental and computed energies.

### 3.3. Nonrigid molecules

In this section we extend our analysis to the rovibrational bending spectrum of nonrigid molecules; species characterized by a low potential energy barrier to linearity. We consider six molecular species: methyl isocyanate ( $\text{CH}_3\text{NCO}$ ), isothiocyanic acid ( $\text{HNCS}$ ), cyanogen isothiocyanate ( $\text{NCNCS}$ ), the isotopologue  $^{37}\text{Cl}$  of chloronitrile oxide ( $^{37}\text{ClCNO}$ ), carbon suboxide ( $\text{OCCCO}$ ), and disilicon carbide ( $\text{Si}_2\text{C}$ ).

These molecules have in common that, depending on the energy window considered, they can display spectroscopic signatures of either bent or linear configurations. Therefore, they showcase the expected patterns for an ESQPT, when the system transforms from a bent to a linear shape, once it overcomes



the potential barrier and explores the previously forbidden linear configuration region of the phase space. Being so rich in spectroscopic features, we need to consider simultaneously interactions from the two dynamical symmetries and, typically, Hamiltonians are more complex than the ones shown in Subsects. 3.1 and 3.2.

For these nonrigid molecules, it is expected that low energy eigenstates should be better defined within the displaced oscillator basis set  $-SO(3)$  dynamical symmetry— whereas states with energies above the potential barrier should be better characterized in the cylindrical oscillator basis set  $-U(2)$  dynamical symmetry. Therefore, depending on the energy, vibrational bending overtones could be assigned either to asymmetric top quantum labels, or to 2D harmonic oscillator quantum labels  $(n, \ell)$  used in the linear case. These two sets of quantum numbers are linked by the transformation (see, e.g., [15]):

$$\begin{aligned}\nu_b &= \frac{n - |\ell|}{2} \\ K_a &= \ell \quad .\end{aligned}\tag{Eq. 18}$$

In this Section, and following the experimental convention, we use the asymmetric top notation for all molecules, even for carbon suboxide (Subsec. 3.3.5), despite the very low barrier that separates it from the linear configuration.

In Tab. 11, we show the optimized parameter values of the 4-body Hamiltonian (Eq. 10), the total vibron number (N), the number of experimental data included in the fit, and the resulting *rms*, labeled as *rms<sub>n</sub>*. For the sake of comparison, we include the *rms* obtained in Refs. [50; 51], *rms<sub>o</sub>*, for those species previously analyzed with the two-body Hamiltonian.

The use of a 4-body Hamiltonian notably improves the fits for methyl isocyanate (CH<sub>3</sub>NCO), isothiocyanic acid (HNCS), cyanogen isothiocyanate (NC-NCS), and the isotopologue <sup>37</sup>Cl of chloronitrile oxide (<sup>37</sup>ClCNO). In the HNCS and <sup>37</sup>ClCNO cases, the *rms* has decreased in one order of magnitude with respect to the former calculation. The results obtained for the OCCCCO and Si<sub>2</sub>C molecules, that were not included in Refs. [50; 51], also display a good agreement with the experimental data.

In this case, most interactions included in the general four-body Hamiltonian (Eq. 10) are needed in the analysis of one or the other nonrigid molecule, with the exception of the  $\hat{n}\hat{\ell}^2$  interaction (parameter  $P_{32}$ ). The energies and eigenstates resulting from the optimized Hamiltonian are used to prepare the quantum monodromy diagram, the Birge-Sponer plot, the PR plot, and the energy functional plot that we present for each molecule.



Molecule	CH <sub>3</sub> NCO	HNCS	NCNCS	<sup>37</sup> CICNO	OCCCO	Si <sub>2</sub> C
$P_{11}$	449.5(13)	539(16)	183.2(21)	758.73(15)	263.99(15)	63.8(5)
$P_{21}$	-5.477(22)	10.3(2.4)	-2.25(4)	-7.8895(23)	-2.3308(25)	-0.108(18)
$P_{22}$	7.85(7)	6.8(6)	0.48(9)	3.85(4)	1.300(17)	0.98(5)
$P_{23}$	-1.628(4)	-9.10(11)	-0.755(7)	-2.1217(6)	-0.6768(4)	-0.8117(17)
$P_{31}$	-	-1.13(10)	-	-	-	-
$P_{33}$	-	-	-	9(7)e-6	-	-
$P_{42}$	-	-	-	-3(3)e-4	-	-
$P_{43}$	-	5.1(3)e-2	-	-	7.2(12)e-4	-
$P_{44}$	-	-	2.30(22)e-4	-	-	-
$P_{45}$	-1.25(23)e-5	-	-	-6.46(14)e-6	-	-
N	78	25	70	92	100	49
$rms_n$	1.10	0.40	1.69	0.095	0.60	1.48
$rms_o$	1.34	3.3	2.18	0.71	-	-
n.dat	19	12	70	33	36	37

Table Tab. 11: Optimized Hamiltonian parameters ( $P_{ij}$ , in  $\text{cm}^{-1}$  units) for nonrigid molecules. Values are given with their associated uncertainty in parentheses in units of the last quoted digits. The total vibron number and the  $rms$  obtained in this work,  $rms_n$ , are also included. For the sake of comparison, the  $rms$  obtained in Refs. [50; 51], if available, is also shown, labeled as  $rms_o$ .

Table Tab. 12: Height of the barrier to linearity and equilibrium deviation to linearity angle obtained from the literature (see footnotes).

Molecule	$E_{ts}(\text{cm}^{-1})$		$\theta_e(^{\circ})$
	This Work	Other Work	Other Work
CH <sub>3</sub> NCO	703.70	928.2(47) <sup>a</sup>	39.977(31) <sup>a</sup>
HNCS	681.75	990.74(35) <sup>b</sup>	48.3 <sup>c</sup>
NCNCS	225.17	270.93(25) <sup>d</sup>	39.017 <sup>d</sup>
<sup>37</sup> CICNO	151.08	166.86(84) <sup>e</sup>	28.71 <sup>e</sup>
OCCCO	17.01	18.3 <sup>f</sup>	24.12 <sup>f</sup>
Si <sub>2</sub> C	675.32	783(48) <sup>g</sup>	65.13 <sup>h</sup>

<sup>a</sup> Ref. [127].

<sup>b</sup> Obtained with the semirigid model from the rotational spectrum in the ground vibrational state. The estimate of the barrier is 900(200)  $\text{cm}^{-1}$  when obtained from the rotational structure of  $\nu_4 = 1$  [128].

<sup>c</sup> Ref. [129].

<sup>d</sup> Ref. [8].

<sup>e</sup> Ref. [130].

<sup>f</sup> Ref. [131].

<sup>g</sup> Ref. [17].

<sup>h</sup> Ref. [132].

### 3.3.1. Methyl isocyanate, CH<sub>3</sub>NCO

Methyl isocyanate has a complex spectrum due to two vibrational modes of large amplitude: an internal CH<sub>3</sub> rotor, with a low energy potential barrier ( $\approx 20 \text{ cm}^{-1}$ ), and the CNC bending mode, characterized by a large anharmonic-



ity [127]. As discussed in Ref. [127], neither a symmetric top basis set plus a degenerate bending CNC mode nor an asymmetric top basis set and a harmonic CNC bending normal mode are enough to reproduce the rovibrational structure of this molecule.

For this reason, the algebraic approach is an interesting alternative for the description of the CNC bending mode; ignoring hereafter the effects of the torsional mode and their interactions, notwithstanding the low barrier of the torsional potential.

Only 19 experimental data, up to  $\nu_b^{max} = 3$  and  $J = 7$ , are available [127]. As shown in Tab. 11, a fit with a Hamiltonian including five parameters from Eq. 10 provides an *rms* of  $1.1 \text{ cm}^{-1}$ . The parameter  $P_{45}$ , which goes with a fourth-order operator combining  $\hat{n}^2$  and  $\hat{W}^2$ , improves lightly the *rms* from the  $1.34 \text{ cm}^{-1}$  value reported in Ref. [50]. The experimental and calculated energy term values are reported in Tab. 13 and the eigenvalues and eigenstates obtained from the algebraic model are used to come up with the different panels of Fig. 10.

From the quantum monodromy diagram in the upper-left panel of Fig. 10 it is clear that the monodromy appears at  $\nu_b = 5$ , around  $900 \text{ cm}^{-1}$ . This is further supported by the Birge-Sponer plot (upper-right panel), which displays a bending mode anharmonicity sign change associated with the potential barrier to linearity –Dixon dip– also around the  $\nu_b = 5$  band. The PR for this molecule (bottom left panel) shows that at low energies the eigenfunctions are more localized in the displaced oscillator basis, until energies around  $800 \text{ cm}^{-1}$ , where the two lines cross and the localization is similar in both bases. The energy functional (bottom-right panel) is plotted using the equilibrium structure provided by [127] to define the scale transformation between the coherent state coordinate and the angle to linearity,  $\theta_e$  (see Tab. 12). The barrier to linearity was estimated to lie at  $928.2(47) \text{ cm}^{-1}$  in Ref. [127] considering a linear NCO chain, whereas the effective barrier to linearity value provided by our model is around  $700 \text{ cm}^{-1}$  (see Tab. 12). As expected, our estimated barrier value is close to the one given by [50] (barrier to linearity,  $728 \text{ cm}^{-1}$ ). It is interesting to highlight that, according to the quantum monodromy, Birge-Sponer, and PR plots in Fig. 10, the potential barrier to linearity should be closer to the value estimated by [127] than the one provided in the classical limit.



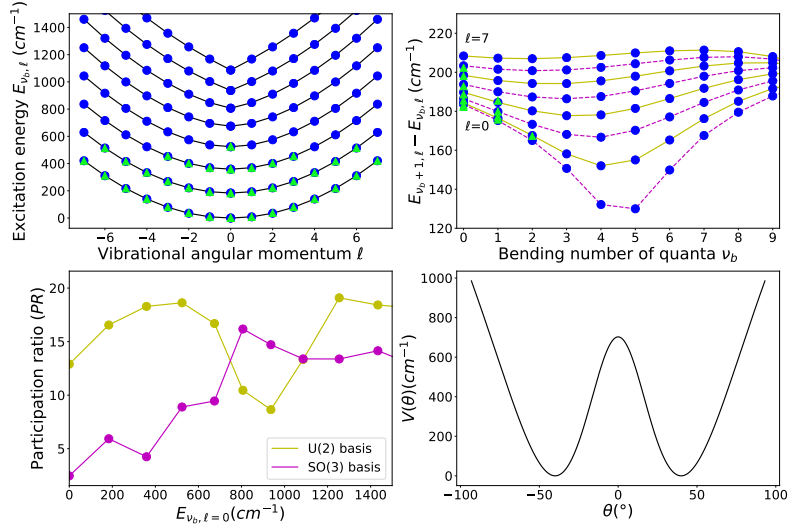


Figure Fig. 10: The upper row includes the quantum monodromy plot (upper left panel) and the Birge-Sponer plot (upper right panel) for CH<sub>3</sub>NCO, using blue circles (green triangles) for calculated (experimental) data. The lower row includes the CH<sub>3</sub>NCO PR for  $\ell = 0$  eigenstates in the two bases considered as a function of the state energy (lower left panel) and the energy functional (lower right panel).



Table Tab. 13: Experimental and calculated term values and residuals for the CNC bending mode of methyl isocyanate. Units of  $\text{cm}^{-1}$ .

$(\nu_b, K_a)^a$	Exp. <sup>b</sup>	Cal. <sup>c</sup>	Exp.-Cal. <sup>d</sup>
( 0 1)	8.4	8.7997	-0.400
( 0 2)	36.8	35.1316	1.668
( 0 3)	80.0	78.8075	1.192
( 0 4)	140.6	139.5489	1.051
( 0 5)	217.5	217.0241	0.476
( 0 6)	311.1	310.8790	0.221
( 0 7)	420.0	420.7589	-0.759
( 1 0)	182.2	183.5477	-1.348
( 1 1)	191.4	193.0995	-1.700
( 1 2)	222.3	221.5793	0.721
( 1 3)	268.6	268.5326	0.067
( 1 4)	333.4	333.3653	0.035
( 1 5)	415.5	415.4570	0.043
( 1 6)	513.4	514.2226	-0.823
( 2 0)	357.9	358.8119	-0.912
( 2 1)	368.6	369.6086	-1.009
( 2 2)	402.1	401.4326	0.667
( 2 3)	454.0	453.1013	0.899
( 3 0)	525.1	523.8246	1.275

<sup>a</sup> Displaced oscillator basis quantum labels assigned to the optimized eigenvectors.

<sup>b</sup> Experimental energies from [127].

<sup>c</sup> Calculated energies.

<sup>d</sup> Difference between experimental and calculated energies.

### 3.3.2. Isothiocyanic acid, HNCS

Isothiocyanic acid (HNCS) is the most stable member of an isomeric family which is also formed by thiocyanic acid (HSCN), thiofulminic acid (HCNS), and isothiofulminic acid (HSNC) [133]. In particular, isothiocyanic acid is a tetratomic nonrigid molecule, with a bent equilibrium structure and a large amplitude HNC bending mode, labeled as  $\nu_4$ . Depending on the reference, some authors consider it either as a quasilinear [129] or a quasibent [51] molecular species. Anyway, this molecule is a perfect candidate to test the algebraic four-body Hamiltonian (Eq. 10).

Up to our knowledge, there are not many available experimental spectral data for this molecular species in the literature, and the existing ones only involve data up to  $K_a^{max} = 7$  from the vibrational ground state and the three fundamental bending bands, i.e., the large amplitude motion,  $\nu_4$ , and the small amplitude NCS-in-plane,  $\nu_5$ , and NCS-out-of-plane,  $\nu_6$ , bend vibration [129; 134].

We perform the analysis of the fundamental and all known overtones of the state  $\nu_4$  (twelve experimental term values), reaching the conclusion that six free spectroscopic parameters in Hamiltonian (Eq. 10) are needed to correctly



reproduce the spectrum. The agreement with the data of the fit is excellent, with an  $rms = 0.4 \text{ cm}^{-1}$  (see Tab. 11). In Tab. 14, we provide experimental and calculated results, and it can be seen how the present study achieves a noticeable improvement with respect to the fit published in [51], with the addition of two extra parameters  $P_{31} (\hat{n}^3)$  and  $P_{43} (\hat{\ell}^4)$ . It should be noted that the first one belongs to the  $U(2)$  subalgebra chain, characteristic of molecular linear configurations, and the second is common to the two chains. The improvement attained with the inclusion of these two interactions could be explained because the bent-to-linear transition is predicted at relatively low energies –the barrier to linearity is around  $680 \text{ cm}^{-1}$  (see the energy functional in Fig. 11 and Tab. 12)– and most experimental data (9 over 12 energies) are located around or above the linearity barrier.

As with the other examples in the paper, we use the eigenvalues and eigenstates predicted by the model to compute the different quantities depicted in the panels of Fig. 11. According to our predictions, the critical energy of the quantum monodromy appears between the  $\nu_4 = 1$  and 2 levels (see upper left panel in Fig. 11). The adjacent energy levels difference in the Birge-Sponer plot show that, for  $\ell = 0$ , the anharmonicity switch from negative to positive, a low energy Dixon dip at  $\nu_4 = 1$ , that can be explained from the influence of the barrier to linearity. As expected, for larger vibrational angular momentum  $\ell$ , the states present the negative anharmonicity typical of bent molecules, due to the centrifugal barrier that prevents the exploration of the origin by the state wavefunctions [41]. The PR results, shown in the lower left panel of Fig. 11, indicate that the available experimental levels can be better described within the cylindrical oscillator basis, where they are slightly more localized. In this case the PR values for both bases are quite close since the fundamental state  $\nu_4 = 1$  is already very close or above the potential barrier.

Therefore, the quantum monodromy diagram and the Birge-Sponer plot at low angular momentum  $\ell$ , further supported by the obtained energy functional, show that this molecular species is nonrigid, with a low energy bent-to-linear transition occurring in the fundamental or first overtone of the  $\nu_4$  bending vibration, despite the PR further supports the quasilinearity notion [129]. The small number of experimental term values hinders the fit in this case, and new experimentally measured energy levels will help improving the present model results. We include our list of predicted levels in the Supplementary Material for the article.



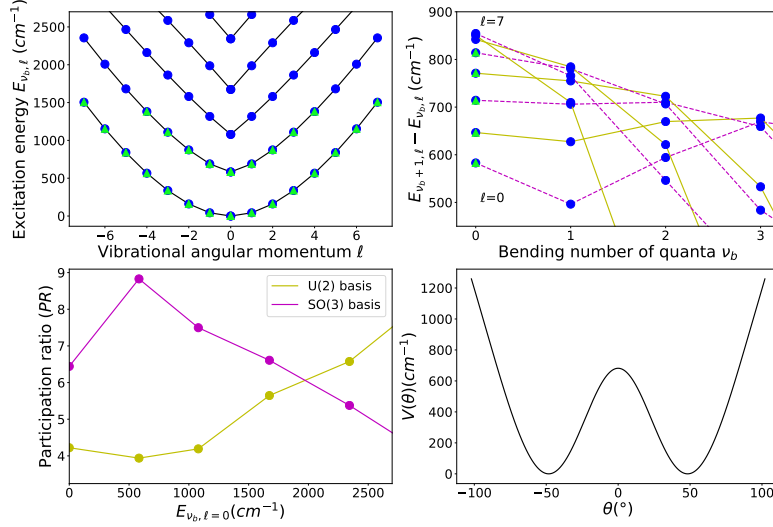


Figure Fig. 11: The upper row includes the quantum monodromy plot (upper left panel) and the Birge-Sponer plot (upper right panel) for the  $\nu_4$  mode of HNCS, using blue circles (green triangles) for calculated (experimental) data. The lower row includes the HNCS PR for  $\ell = 0$  eigenstates in the two bases considered as a function of the state energy (lower left panel) and the energy functional derived using the coherent state formalism (lower right panel)-

Table Tab. 14: Experimental and calculated term values and residuals for the  $\nu_4$  mode of isothiocyanid acid bending mode. Units of cm<sup>-1</sup>.

$(\nu_b, K_a)^a$	Exp. <sup>b</sup>	Cal. <sup>c</sup>	Exp.-Cal. <sup>d</sup>
(0 1)	43.49	42.9862	0.504
(0 2)	160.30	159.9050	0.395
(0 3)	337.44	337.5577	-0.118
(0 4)	565.89	566.2625	-0.372
(0 5)	839.36	839.4430	-0.083
(0 6)	1153.33	1152.9362	0.394
(0 7)	1504.36	1504.5071	-0.147
(1 0)	582.90	582.8427	0.057
(1 1)	689.66	689.6294	0.031
(1 2)	873.89	874.1977	-0.308
(1 3)	1109.07	1108.7203	0.350
(1 4)	1380.21	1380.3289	-0.119

<sup>a</sup> Displaced oscillator basis quantum labels assigned to the optimized eigenvectors.

<sup>b</sup> Experimental energies from [129; 134].

<sup>c</sup> Calculated energies.

<sup>d</sup> Difference between experimental and calculated energies.



### 3.3.3. Cyanogen isothiocyanate, $NCNCS$

Cyanogen isothiocyanate is a quasilinear molecule [135], a label that stems from its large amplitude CNC bending mode, denoted as  $\nu_7$ . The bending spectrum for this mode has been carefully charted in the microwave and millimeter ranges for several highly-excited  $\nu_7$  states and this molecule has been subject of several works aiming to study quantum monodromy effects [8; 135]. In fact, this molecule is one of the best examples of quantum monodromy found to date [13].

In this work we analyze all experimental term values up to  $\nu_b = \nu_7 = 6$  and  $K_a = 9$  reported in [13]. Seventy experimental data have been fitted using 5 parameters of the four-body Hamiltonian (Eq. 10), with a final  $rms=1.69\text{ cm}^{-1}$  (see Tab. 11), which lightly improves the  $rms$  of  $2.2\text{ cm}^{-1}$  obtained in [50]. This improvement is achieved thanks to the inclusion of a four-body interaction,  $\hat{\ell}^2\hat{W}^2$ .

The experimental and calculated energies are reported in Tab. 15 and the four quantities of interest considered in the present work are depicted in Fig. 12. The quantum monodromy plot, in the upper left panel, and the Birge-Sponer plot, in the upper right panel, indicate that the critical energy of the monodromy (or the ESQPT critical energy) appears at  $\nu_b = 3$ , in agreement with the literature [13; 15; 50]. The PR, plotted in the lower left panel, makes evident the lack of significant localization effects in any basis for energies below the barrier. Nevertheless, the closest eigenstate to the critical energy  $-\nu_b = 3$  overtone— is significantly more localized in the cylindrical oscillator basis, as expected from recent findings [49; 56; 57].

The energy functional for this molecule, in the lower right panel of Fig. 12, allows for the estimation of the linearity barrier at  $225\text{ cm}^{-1}$  (see Tab. 12), which is in better agreement with the  $217\text{ cm}^{-1}$  value of [50] than with the value  $270.93(25)\text{ cm}^{-1}$  provided by [8]. Therefore, according to Fig. 12, this study highlights that this molecule is a nonrigid bent molecule which undergoes a bent-to-linear transition, in consonance with [13; 15].



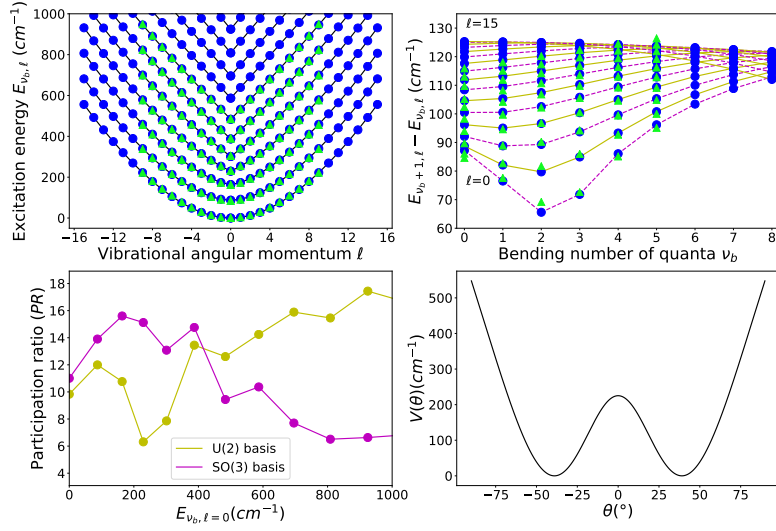


Figure Fig. 12: The upper row shows the quantum monodromy plot (upper left panel) and the Birge-Sponer plot (upper right panel) for the  $\nu_7$  bending mode of NCNCS, using blue circles (green triangles) for calculated (experimental) data. The lower row includes the PR for  $\ell = 0$  eigenstates in the two bases considered as a function of the state energy (lower left panel) and the bending energy functional derived using the coherent state formalism (lower right panel).



Table Tab. 15: Experimental and calculated energy term values and residuals for the  $\nu_7$  bending mode of cyanogen isothiocyanate. Units of  $\text{cm}^{-1}$ .

$(\nu_b, K_a)^a$	Exp. <sup>b</sup>	Cal. <sup>c</sup>	Exp.-Cal. <sup>d</sup>	$(\nu_b, K_a)^a$	Exp. <sup>b</sup>	Cal. <sup>c</sup>	Exp.-Cal. <sup>d</sup>
(0 0)	0.0	0.0000	0.000	(3 5)	391.7	391.7179	-0.018
(0 1)	3.6	3.1840	0.416	(3 6)	434.1	434.3698	-0.270
(0 2)	13.9	12.5762	1.324	(3 7)	479.1	479.8865	-0.787
(0 3)	30.2	27.8237	2.376	(3 8)	526.4	528.1226	-1.723
(0 4)	51.9	48.5265	3.373	(3 9)	575.9	578.9448	-3.045
(0 5)	78.3	74.3091	3.991	(4 0)	304.0	301.1481	2.852
(0 6)	110.0	104.8419	5.158	(4 1)	340.1	338.6773	1.423
(0 7)	143.3	139.8406	3.459	(4 2)	376.9	376.5042	0.396
(0 8)	181.0	179.0596	1.940	(4 3)	416.1	416.1141	-0.014
(0 9)	221.8	222.2848	-0.485	(4 4)	457.6	457.8967	-0.297
(1 0)	84.6	87.2126	-2.613	(4 5)	501.5	501.9531	-0.453
(1 1)	89.7	91.9233	-2.223	(4 6)	547.6	548.2809	-0.681
(1 2)	103.6	104.6835	-1.084	(4 7)	595.8	596.8334	-1.033
(1 3)	124.2	124.0460	0.154	(4 8)	646.1	647.5419	-1.442
(1 4)	150.2	149.0112	1.189	(4 9)	698.2	700.3252	-2.125
(1 5)	180.7	178.9069	1.793	(5 0)	389.1	387.2173	1.883
(1 6)	215.2	213.2607	1.939	(5 1)	432.8	431.9699	0.830
(1 7)	253.0	251.7215	1.278	(5 2)	476.3	476.1711	0.129
(1 8)	294.0	294.0143	-0.014	(5 3)	520.7	521.1156	-0.416
(1 9)	337.7	339.9134	-2.213	(5 4)	566.8	567.3528	-0.553
(2 0)	162.2	163.7232	-1.523	(5 5)	614.5	615.1264	-0.626
(2 1)	172.4	174.0334	-1.633	(5 6)	664.0	664.5363	-0.536
(2 2)	192.5	193.4916	-0.992	(5 7)	715.2	715.6078	-0.408
(2 3)	218.8	219.0777	-0.278	(5 8)	768.2	768.3234	-0.123
(2 4)	249.9	249.5584	0.342	(5 9)	822.7	822.6384	0.062
(2 5)	284.9	284.2788	0.621	(6 0)	484.2	483.4009	0.799
(2 6)	323.4	322.8248	0.575	(6 1)	532.8	532.7402	0.060
(2 7)	364.9	364.9014	-0.001	(6 2)	581.1	581.4825	-0.382
(2 8)	409.1	410.2795	-1.179	(6 3)	629.8	630.4893	-0.689
(2 9)	455.7	458.7694	-3.069	(6 4)	679.6	680.2337	-0.634
(3 0)	231.4	229.3102	2.090	(6 5)	730.7	730.9713	-0.271
(3 1)	254.1	253.7520	0.348	(6 6)	783.2	782.8331	0.367
(3 2)	282.7	282.7951	-0.095	(6 7)	837.1	835.8753	1.225
(3 3)	315.6	315.7031	-0.103	(6 8)	892.4	890.1058	2.294
(3 4)	352.1	352.0963	0.004	(6 9)	949.1	945.5006	3.599

<sup>a</sup> Displaced oscillator basis quantum labels assigned to the optimized eigenvectors.

<sup>b</sup> Experimental energies from [13].

<sup>c</sup> Calculated energies.

<sup>d</sup> Difference between experimental and calculated energies.



### 3.3.4. $^{37}\text{Cl}$ isotopologue of chloronitrileoxide, $^{37}\text{ClCNO}$

In this case, there are experimental data on the rotational lines for the CNO bending,  $\nu_4$ , and ClCN bending,  $\nu_5$  for the main isotopologue and the isotopologue  $^{37}\text{Cl}$  of chloronitrileoxide ( $^{35}\text{ClCNO}$  and  $^{37}\text{ClCNO}$ , respectively) [130]. The molecule is considered as a quasilinear species due to the large amplitude vibrations of the  $\nu_5$  bending mode [13; 130].

We have included in our analysis all available  $\nu_5$  mode experimental data for the isotopologue  $^{37}\text{Cl}$ , up to  $\nu_b = \nu_5 = 3$  and  $\ell = 9$ . A set of thirty-three experimental term values have been fitted, with seven free parameters in the Hamiltonian of Eq. 10. The free parameters include the parameters for one- and two-body interactions, one three-body parameter,  $P_{33}$ , and two parameters associated with four-body terms,  $P_{42}$  and  $P_{45}$ . The final result is an *rms* of  $0.09\text{ cm}^{-1}$  (see Tab. 11), managing to reduce the *rms* of the two-body Hamiltonian fit in one order of magnitude [50]. The calculations are compared with the experimental rovibrational energy levels (Tab. 16) and they are, in general, very close to, or below, experimental accuracy. The obtained eigenvalues and eigenstates have been used to prepare Fig. 13.

According to the quantities plot in Fig. 13, the  $^{37}\text{ClCNO}$  molecule has a low barrier to linearity and the critical energy in the quantum monodromy diagram shows up already for  $\nu_5 = 1$ . The Birge-Sponer plot further supports this fact with a positive anharmonicity from the ground state on. This is a trait common to other quasilinear molecules (e.g. see Subsec. 3.1.1). The quantum monodromy diagram –upper left panel– reveals that the linearity barrier is close to, or even under, vibrational band  $\nu_5 = 1$ . The Birge-Sponer plot –upper right panel– does not include a Dixon dip, though there is a significant change of slope for  $\nu_5 = 1$ . However, the PR –lower left panel of Fig. 13– evinces a maximum localization for states up to  $\nu_5 = 1, 2$  in the cylindrical oscillator basis set, which is an evidence supporting that the critical energy of the ESQPT (or of the quantum monodromy) is located between these two term values and the quasilinear condition of  $^{37}\text{ClCNO}$ . State  $\nu_5 = 3$  is equally localized in the  $U(2)$  or  $SO(3)$  basis sets. However, from  $\nu_5 = 4$  up, there is an enhanced localization in the displaced oscillator basis. In this work, the energy functional –lower right panel of Fig. 13– brings to an estimate of the linearity barrier equals to  $151.08\text{ cm}^{-1}$ . From our results, the  $\nu_5$  bending fundamental is just below the maximum. The present result is in good agreement with the estimation obtained with the semi-rigid bender model, with a value of the linearity barrier of  $166.9\text{ cm}^{-1}$  [130]. It is also in good accordance with the previously reported algebraic estimate with a two-body Hamiltonian: a potential barrier of  $140\text{ cm}^{-1}$  [50].



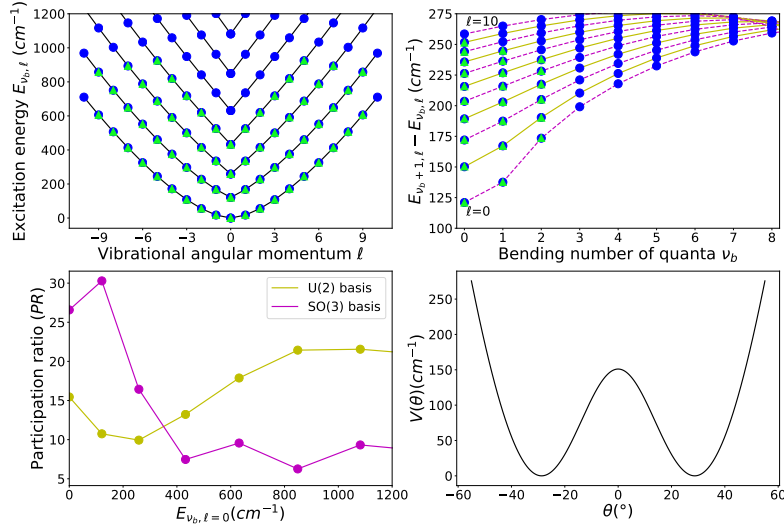


Figure Fig. 13: The upper row shows the quantum monodromy plot (upper left panel) and the Birge-Sponer plot (upper right panel) for the  $\nu_5$  bending mode of  $^{37}\text{ClCNO}$ , using blue circles (green triangles) for calculated (experimental) data. The lower row includes the PR for  $\ell = 0$  eigenstates in the two bases considered as a function of the state energy (lower left panel) and the bending energy functional derived using the coherent state formalism (lower right panel).



Table Tab. 16: Experimental and calculated term values and residuals for the  $\nu_5$  bending mode of the isotopologue  $^{37}\text{Cl}$  of chloronitrileoxide ( $^{37}\text{ClCNO}$ ). Units of  $\text{cm}^{-1}$ .

$(\nu_b, K_a)^a$	Exp. <sup>b</sup>	Cal. <sup>c</sup>	Exp.-Cal. <sup>d</sup>
( 0 1)	17.5	17.5692	-0.069
( 0 2)	55.6	55.6451	-0.045
( 0 3)	108.1	108.1468	-0.047
( 0 4)	171.8	171.8459	-0.046
( 0 5)	244.7	244.7436	-0.044
( 0 6)	325.4	325.4799	-0.080
( 0 7)	413.1	413.0690	0.031
( 0 8)	506.8	506.7617	0.038
( 0 9)	606.1	605.9690	0.131
( 1 0)	120.9	120.9833	-0.083
( 1 1)	167.9	167.7603	0.140
( 1 2)	227.8	227.6535	0.147
( 1 3)	297.6	297.4398	0.160
( 1 4)	375.5	375.4279	0.072
( 1 5)	460.5	460.4970	0.003
( 1 6)	551.8	551.8276	-0.028
( 1 7)	648.7	648.7857	-0.086
( 1 8)	750.8	750.8622	-0.062
( 1 9)	857.6	857.6366	-0.037
( 2 0)	258.5	258.5753	-0.075
( 2 1)	335.1	335.0054	0.095
( 2 2)	415.1	415.0632	0.037
( 2 3)	500.5	500.4749	0.025
( 2 4)	591.3	591.3146	-0.015
( 2 5)	687.2	687.3197	-0.120
( 2 6)	788.1	788.1610	-0.061
( 2 7)	893.5	893.5127	-0.013
( 3 0)	432.0	432.0547	-0.055
( 3 1)	525.3	525.4014	-0.101
( 3 2)	620.1	620.1432	-0.043
( 3 3)	717.9	717.9974	-0.097
( 3 4)	819.6	819.5132	0.087
( 3 5)	925.0	924.8061	0.194

<sup>a</sup> Displaced oscillator basis quantum labels assigned to the optimized eigenvectors.

<sup>b</sup> Experimental energies from [130].

<sup>c</sup> Calculated energies.

<sup>d</sup> Difference between experimental and computed energies.

### 3.3.5. Carbon suboxide, *OCCCO*

Experiments using MW, IR, and Raman spectroscopy of carbon suboxide has provided a number of spectral data for all the vibrational modes (see e.g. [136; 137; 138]). Among them, we focus on the CCC bending mode, labeled



as  $\nu_7$ , that displays evidences of large amplitude motion. In this case, the low barrier to linearity places this molecular species quite close to the linear limit, and it has been classified as a quasilinear molecule in other works [15].

Our analysis uses all the available experimental energies, a set that include data from the first twelve excited bands of  $\nu_7$  (which corresponds to  $n = 12$  in the linear quantum number notation) and with a maximum vibrational angular momentum of  $\ell = 12$ . These energies have been obtained from IR and Raman measurements [136; 138].

The fit of the 36 available experimental energies with the four parameters of the two-body Hamiltonian (Eq. 9) has an  $rms=1.03 \text{ cm}^{-1}$ . The inclusion of higher order interactions from the four-body Hamiltonian (Eq. 10) improves the  $rms$  to  $0.60 \text{ cm}^{-1}$  with the addition of a single extra parameter associated with a four-body interaction,  $P_{43}(\ell^4)$  (Tab. 11). Tab. 17 shows the fine agreement between calculated and experimental term values, labeled with the bent molecule quantum numbers,  $(\nu_7, K_a)$ .

From the calculated eigenstates and eigenvalues, we have computed the quantities shown in the four panels of Fig. 14 where, according to Eq. 18, the maximum number of excitation quanta in the experimental energies is  $\nu_7 = 3$ . All the quantities shown in this figure point towards the consideration of this bending mode as a quasilinear one. The small value of the barrier to linearity has as consequence that the ground state is the only state below the linearity barrier. In this case, the low barrier prevents the appearance of a Dixon dip in the Birge-Sponer plot –upper right panel–, where anharmonicities are positive for all number of quanta, a distinctive feature of quasilinear molecules. The PR plot –lower left panel– evinces a very slight localization between the ground state and the first fundamental, that can be explained to the low barrier value. At least up to  $\nu_b = 5$ , inclusive, the cylindrical oscillator basis set (in correspondence with a linear configuration) is more suitable than the bent  $SO(3)$  basis set and as energy grows both bases give similar results.

The estimate of the linearity barrier from the energy functional obtained with the coherent states approach –lower right panel of Fig. 14– is  $17.01 \text{ cm}^{-1}$  (Tab. 12). This value is in agreement with the results obtained with the semirigid bender model [131]. According to our results, it can be concluded that this molecule is a nonrigid species. However, due to the low barrier value, some authors support the convenience of labeling the vibrational energies of this mode of carbon suboxide with the cylindrical oscillator basis quantum numbers  $(n, \ell)$  rather than with that of the bent configuration [136; 138].



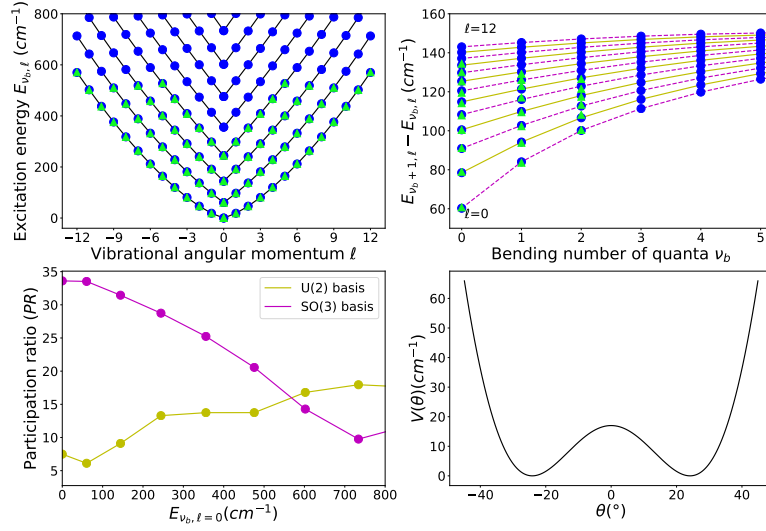


Figure Fig. 14: The upper row shows the quantum monodromy plot (upper left panel) and the Birge-Sponer plot (upper right panel) for the  $\nu_7$  bending mode of OCCO, using blue circles (green triangles) for calculated (experimental) data. The lower row includes the PR for  $\ell = 0$  eigenstates in the two bases considered as a function of the state energy (lower left panel) and the bending energy functional derived using the coherent state formalism (lower right panel).



Table Tab. 17: Experimental and calculated term values and residuals for the  $\nu_7$  bending mode of carbon suboxide. Units of  $\text{cm}^{-1}$ .

$(\nu_b, K_a)^a$	Exp. <sup>b</sup>	Cal. <sup>c</sup>	Exp.-Cal. <sup>d</sup>	$(\nu_b, K_a)^a$	Exp. <sup>b</sup>	Cal. <sup>c</sup>	Exp.-Cal. <sup>d</sup>
(0 1)	18.26	18.6992	-0.439	(1 6)	331.89	332.2362	-0.346
(0 2)	46.11	46.5077	-0.398	(1 7)	388.95 <sup>e</sup>	388.5720	0.378
(0 3)	80.62	80.7562	-0.136	(1 8)	447.91 <sup>e</sup>	447.7649	0.145
(0 4)	120.37	120.1677	0.202	(1 9)	510.04 <sup>e</sup>	509.7910	0.249
(0 5)	164.49	163.9969	0.493	(2 0)	144.30	144.3237	-0.024
(0 6)	212.39	211.7697	0.620	(2 1)	191.06	191.4047	-0.345
(0 7)	263.65	263.1754	0.475	(2 2)	239.57 <sup>e</sup>	240.1833	-0.613
(0 8)	317.94	318.0129	-0.073	(2 3)	290.52 <sup>e</sup>	291.1648	-0.645
(0 9)	375.65 <sup>e</sup>	376.1611	-0.511	(2 4)	345.27 <sup>e</sup>	344.4932	0.777
(0 10)	436.77 <sup>e</sup>	437.5605	-0.790	(2 5)	401.59 <sup>e</sup>	400.2001	1.390
(0 11)	501.91 <sup>e</sup>	502.2016	-0.292	(2 6)	458.01 <sup>e</sup>	458.2888	-0.279
(0 12)	570.68 <sup>e</sup>	570.1176	0.562	(2 7)	518.15 <sup>e</sup>	518.7647	-0.615
(1 0)	60.70	60.2641	0.436	(3 0)	244.70 <sup>e</sup>	244.4933	0.207
(1 1)	97.22	97.2064	0.014	(3 1)	299.26 <sup>e</sup>	298.0714	1.189
(1 2)	137.26	137.4456	-0.186	(3 2)	352.91 <sup>e</sup>	352.8682	0.042
(1 3)	181.02	181.2484	-0.228	(3 3)	407.97 <sup>e</sup>	409.2405	-1.270
(1 4)	228.23	228.4401	-0.210	(3 4)	466.79 <sup>e</sup>	467.3687	-0.579
(1 5)	278.61	278.8222	-0.212	(3 5)	528.08 <sup>e</sup>	527.3550	0.725

<sup>a</sup> Cylindrical oscillator basis quantum labels assigned to the optimized eigenvectors.

<sup>b</sup> Experimental energies from [138] unless noted otherwise.

<sup>c</sup> Calculated energies.

<sup>d</sup> Difference between experimental and computed energies.

<sup>e</sup> Experimental energies obtained from Raman spectroscopy [136].

### 3.3.6. Disilicon carbide, $\text{Si}_2\text{C}$

Disilicon carbide is a floppy triatomic molecule [139; 140] which, in last years, has been the subject of a number of experimental works on its rotational and rovibrational spectra [17; 132] mostly motivated by the relevance of silicon and carbon clusters in astronomy and in technical applications.

The large amplitude motion of  $\text{Si}_2\text{C}$  stems from the  $\nu_2$  bending mode. All the available experimental rovibrational term values of the excited  $\nu_2$  bands, up to  $\nu_b = \nu_2 = 13$  and  $\ell = 3$  (approx. up to  $1600 \text{ cm}^{-1}$ ) [17], have been considered in the present work. The free parameters in the analysis are four, they include the one- and two-body operators of Eq. 9, and have been fitted to reproduce a total of 37 available experimental data with an *rms* of  $1.48 \text{ cm}^{-1}$  (see Tab. 11). Note that this result is slightly less than the experimental uncertainty of  $2 \text{ cm}^{-1}$  [17] and it represents a considerable improvement when compared with previous works [17; 141]. The calculated energies, labeled with displaced oscillator (bent molecule) quantum numbers, are reported in Tab. 18, together with the experimental data and fit residuals.

The calculated energies and bending eigenstates have been used to compute the different quantities displayed in Fig. 15. The quantum monodromy diagram



–upper left panel– and the Birge-Sponer plot –upper right panel– are in very good accordance with the results published in Refs. [17; 141]. The critical ESQPT energy and the Dixon dip appear at  $\nu_b = 6$ , with a barrier to linearity that extends up to around  $700 \text{ cm}^{-1}$ . The PR results, depicted in the lower left panel, imply a slightly larger eigenstate localization when they are expressed in the displaced oscillator basis, and how the trend is reversed for higher energy values. In particular, this plot illustrates vividly for a number of excitation quanta of  $\nu_b = 6$  the predicted localization effects at the critical ESQPT energy; the states closest to the critical energy have a very large component in the  $|n = 0^{\ell=0}\rangle$  basis state [49; 56; 57]. The energy functional is given in the lower right panel in the figure. The barrier to linearity (Tab. 12) is reckoned at  $675.32 \text{ cm}^{-1}$ , a value which is in relatively good agreement with the one derived  $783(48) \text{ cm}^{-1}$  from the information of the Dixon dip [17] and the value of  $832 \text{ cm}^{-1}$  obtained using *ab initio* calculations [141]. So, the displays in Fig. 15 shows that disilicon carbide can be classified as a nonrigid molecule.

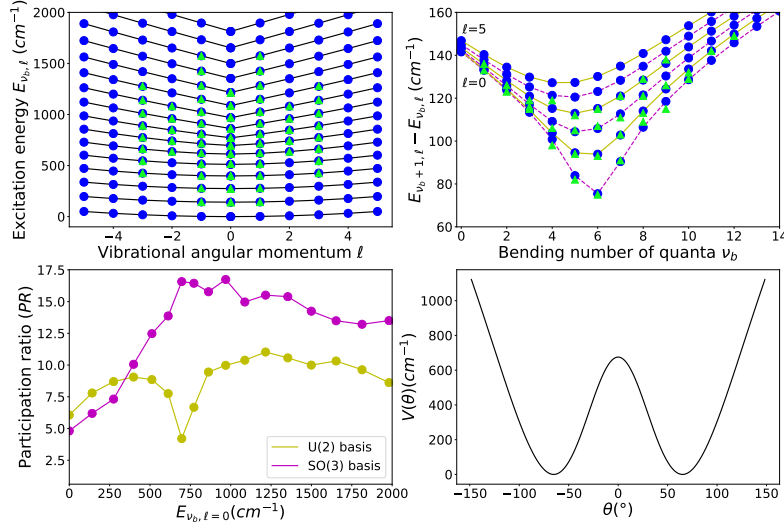


Figure Fig. 15: The upper row shows the quantum monodromy plot (upper left panel) and the Birge-Sponer plot (upper right panel) for the  $\text{Si}_2\text{C}$  bending mode, using blue circles (green triangles) for calculated (experimental) data. The lower row includes the PR for  $\ell = 0$  eigenstates in the two bases considered as a function of the state energy (lower left panel) and the bending energy functional derived using the coherent state formalism (lower right panel).



Table Tab. 18: Experimental and calculated term values and residuals for the bending mode of disilicon carbide. Units of  $\text{cm}^{-1}$ .

$(\nu_b, K_a)^a$	Exp. <sup>b</sup>	Cal. <sup>c</sup>	Exp.-Cal. <sup>d</sup>
(1 0)	140.0	141.5931	-1.593
(1 1)	142.0	143.8421	-1.842
(2 0)	273.0	274.6069	-1.607
(2 1)	278.0	277.1851	0.815
(3 0)	399.0	398.3725	0.627
(3 1)	401.0	401.4841	-0.484
(3 3)	425.0	425.7597	-0.760
(4 0)	515.0	511.7915	3.209
(4 1)	516.0	515.9391	0.061
(4 3)	544.0	546.6778	-2.678
(5 0)	613.0	612.6117	0.388
(5 1)	622.0	619.6988	2.301
(5 2)	636.0	637.0290	-1.029
(5 3)	663.0	661.9059	1.094
(6 0)	695.0	696.4984	-1.498
(6 1)	716.0	714.2134	1.787
(6 2)	741.0	741.3982	-0.398
(6 3)	775.0	774.8380	0.162
(7 0)	770.0	771.9460	-1.946
(7 1)	809.0	808.0725	0.928
(7 2)	848.0	847.2296	0.770
(7 3)	890.0	890.0296	-0.030
(8 0)	861.0	862.3533	-1.353
(8 1)	912.0	910.8638	1.136
(8 2)	959.0	959.9006	-0.901
(8 3)	1011.0	1011.0350	-0.035
(9 0)	970.0	968.8106	1.189
(9 1)	1025.0	1024.8626	0.137
(9 2)	1080.0	1081.3839	-1.384
(9 3)	1140.0	1139.4754	0.525
(10 0)	1085.0	1087.2974	-2.297
(10 1)	1151.0	1149.1694	1.831
(10 3)	1278.0	1275.7166	2.283
(11 0)	1214.0	1215.9113	-1.911
(11 1)	1283.0	1282.7567	0.243
(12 1)	1425.0	1424.8196	0.180
(13 1)	1574.0	1574.7200	-0.720

<sup>a</sup> Displaced oscillator basis quantum labels assigned to the optimized eigenvectors.

<sup>b</sup> Experimental energies from [17].

<sup>c</sup> Calculated energies.

<sup>d</sup> Difference between experimental and computed energies.



## 4. Summary and Conclusions

We use the 2DVM most general Hamiltonian that includes up to four-body interactions to analyze bending vibrations for fourteen different molecules. The molecules have been selected taking into account not only the existence in the literature of enough experimental information to allow for a well converged and physically significant fit, but also trying to consider examples for the different dynamics that can be associated to this interesting vibrational degree of freedom. One of the major advantages of the 2DVM is, apart from its computational simplicity, that such a simple model encompasses systems that range from the linear to bent, including the spectroscopic feature-rich quasilinear and nonrigid cases. We have focused particularly in the nonrigid cases, where an ESQPT associated with a bent-to-linear structural change in the system for increasing excitation energies.

This work can be considered a sequel of Refs. [50; 51], where a systematic study of bending dynamics in systems with ESQPT was performed for the first time. We use a higher-order Hamiltonian to repeat the analysis, incorporating new experimental data when possible, and trying to improve the results and cast some light upon the modeled physical systems. With this aim, the present study provides the characterization of the bending-rotation structure for a set of molecular species which cover all the possible gamut of molecular configurations, including four linear and quasilinear molecules, three of them previously studied in [50; 51] (fulminic acid, hydrogen cyanide, and hydrogen isocyanide) plus a new one (cyanofulminate); four bent molecules, two of them previously studied in [50; 51] (hydrogen sulfide and hydrogen selenide) and two new ones (silylene and ozone); and, finally, six nonrigid species, four of them included among the cases studied in [50; 51] (methyl isocyanate, isothiocyanic acid, cyanogen isothiocyanate, and the isotopologue  $^{37}\text{Cl}$  of chloronitrile oxide) plus two new molecules (carbon suboxide and disilicon carbide). In some of the cases the improvement is very significant ( $\text{HNC}$ ,  $\text{H}_2\text{S}$ ,  $\text{H}_2\text{Se}$ ,  $\text{HNCS}$  and  $^{37}\text{ClCNO}$ ). We have revisited other cases previously included in Refs. [50; 51], but the addition of higher-order terms to the Hamiltonian did not involve significant improvements in the fit when compared to the published results.

The 2DVM model has proved able to deal with large and small amplitude bending motions and, in the particular case of bent molecules, the results have greatly benefited from the inclusion of the coupling with the rotational projection around the molecule-fixed  $z$ -axis in the Hamiltonian. In this work, an extension of the Hamiltonian up to four-body interactions has been systematically applied for the first time to a large set of molecules. This extension has permitted us to model the available experimental data for the fourteen species considered and, according to the *rms* of the fits (see Tab. 1, Tab. 6, and Tab. 11), we obtain in general a fine agreement between experimental and calculated energies. Thus, we consider proved that the 4-body 2DVM Hamiltonian is a suitable effective Hamiltonian for the analysis of a bending vibrations for both small and large amplitude and provides new venues to further explore the ESQPT that occurs in the excitation spectrum of nonrigid molecular species.



As a result of our fits, the model provides predictions for yet unknown highly excited rovibrational energy levels and the wave functions of such states. The value of these levels is provided in the tables enclosed as supplementary information to this paper. This information has been used to provide for each molecule the quantum monodromy diagram, the Birge-Sponer plot, and the participation ratio as a function of the state energy in the two bases provided by the model dynamical symmetries. These results allow for an easier classification of the bending degree of freedom among the possible situations existing between the linear and bent limits, apart from being of great help in the assignment of quantum labels to highly-excited bending states, often quite a cumbersome task.

We also make use of the intrinsic state formalism to compute the classical limit of the model and obtain an energy functional for the bending degree of freedom. Given the level of abstraction of the model, developed far from the traditional approach in phase space, this is a useful contribution, notwithstanding the  $1/N$  approximation level, because the obtained sketches of the bending energy functional for the molecular bending mode shed light on the height of the linearity barriers and the positions and number of minima. Though our predicted barrier to linearity value in some nonrigid molecules does not fully agree with the estimates of other procedures, the obtained values satisfactorily explain the effect on the available rovibrational experimental data of the barrier to linearity. In particular, in the case of bent molecules, the lack of experimental information on very highly-excited energy levels, close to the potential barrier, prevents the inclusion of interactions from the linear dynamical symmetry which hinders the prediction of the energy barrier height. This is a situation similar to the one solved in Refs. [54; 70] where, due to the lack of experimental data at high energies, a set of spectroscopically assigned *ab initio* term values is used. The inclusion of term levels at higher excitation energies will greatly improve the obtained estimates of the barrier to linearity value in such cases.

As a final remark, with the inclusion of the higher order terms, we consider the effective Hamiltonian reported in this work as a valid and computationally inexpensive approach that can compete with other existing approaches, computationally more demanding, for the characterization of the bending mode of molecules with linear, bent, quasilinear, or nonrigid behavior. The programming codes are available upon request to the authors, and they will be published soon [83]. We provide predicted values for highly-excited term values with the hope that they could be of help in the measurement of new experimental values. This is of particular importance in the case of nonrigid molecular species, where an improved knowledge of the critical energy region of the quantum monodromy –and the ESQPT– is of major importance and where our approach could ease the assignment of quantum labels in such systems. Further developments of the model are currently being considered, in particular the possibility of extending the model to treat simultaneously two isomers, using a configuration mixing formalism akin to the one that has been successfully applied to nuclear systems or the coupling of the bending degree of freedom with stretching or other degrees of freedom, including large amplitude ones, are planned in a near future.



*Acknowledgment.* We thank useful discussion with Profs. Francesco Iachello, Renato Lemus, and Georg Mellau. This project has received funding from the European Union's Horizon 2020 research and innovation program under the Marie Skłodowska-Curie grant agreement No 872081 and from the Spanish National Research, Development, and Innovation plan (RDI plan) under the project PID2019-104002GB-C21. This work has also been partially supported by the Consejería de Conocimiento, Investigación y Universidad, Junta de Andalucía and European Regional Development Fund (ERDF), ref. SOMM17/6105/UGR, by the Ministerio de Ciencia, Innovación y Universidades (ref.COOPB20364), and by the Centro de Estudios Avanzados en Física, Matemáticas y Computación (CEAFMC) of the University of Huelva. JKR thanks support from the Youth Employment Initiative and the Youth Guarantee program supported by the European Social Fund. FPB and JKR thank the obtained support from the project UHU-1262561. Computing resources supporting this work were provided by the CEAFMC and Universidad de Huelva High Performance Computer (HPC@UHU) located in the Campus Universitario el Carmen and funded by FEDER/MINECO project UNHU-15CE-2848.

## Appendix A. Operator Matrix elements

### Appendix A.0.1. Operator Matrix Elements in the Dynamical Symmetry (I)

The diagonal operators in this dynamical symmetry are

**Operator  $\hat{n}^p$**  :  $\langle [N]; n^\ell | \hat{n}^p | [N]; n^\ell \rangle = n^p$  for  $p = 1, 2, 3, 4$ .

**Operator  $\hat{\ell}^{2q}$**  :  $\langle [N]; n^\ell | \hat{\ell}^{2q} | [N]; n^\ell \rangle = \ell^{2q}$  for  $q = 1, 2$ .

**Operator  $\hat{n}^p \hat{\ell}^{2q}$**  :  $\langle [N]; n^\ell | \hat{n}^p \hat{\ell}^{2q} | [N]; n^\ell \rangle = n^p \ell^{2q}$  for  $p = 1, 2$  and  $q = 1$ .

The non-diagonal matrix elements in this basis are

**$SO(3)$  Casimir Operator  $\hat{W}^2$**  :

$$\begin{aligned} \langle [N]; n_2^\ell | \hat{W}^2 | [N]; n_1^\ell \rangle = & \left[ (N - n_1)(n_1 + 2) + (N - n_1 + 1)n_1 + \ell^2 \right] \delta_{n_2, n_1} \\ & - \sqrt{(N - n_1 + 2)(N - n_1 + 1)(n_1 + \ell)(n_1 - \ell)} \delta_{n_2, n_1 - 2} \\ & - \sqrt{(N - n_1)(N - n_1 - 1)(n_1 + \ell + 2)(n_1 - \ell + 2)} \delta_{n_2, n_1 + 2} . \end{aligned}$$

Note that this is the main non-diagonal operator in this case and it is a band matrix as the non-zero matrix elements are located in the main and first diagonals only.

**Operator  $\hat{n} \hat{W}^2 + \hat{W}^2 \hat{n}$**  : As the operator  $\hat{n}$  is diagonal the matrix is also band diagonal with matrix elements



$$\begin{aligned}\langle [N]; n_2^\ell | \hat{n} \hat{W}^2 + \hat{W}^2 \hat{n} | [N]; n_1^\ell \rangle = & 2n_1 [(N - n_1)(n_1 + 2) + (N - n_1 + 1)n_1 + \ell^2] \delta_{n_2, n_1} \\ & - (2n_1 - 2) \sqrt{(N - n_1 + 2)(N - n_1 + 1)(n_1 + \ell)(n_1 - \ell)} \delta_{n_2, n_1 - 2} \\ & - (2n_1 + 2) \sqrt{(N - n_1)(N - n_1 - 1)(n_1 + \ell + 2)(n_1 - \ell + 2)} \delta_{n_2, n_1 + 2} .\end{aligned}$$

**Operator  $\hat{\ell}^2 \hat{W}^2$**  : This operator is computed for  $\ell \neq 0$  multiplying the  $\hat{W}^2$  operator matrix times  $\ell^2$ .

**Operator  $\hat{n}^2 \hat{W}^2 + \hat{W}^2 \hat{n}^2$**  : This is computed as the  $\hat{n} \hat{W}^2 + \hat{W}^2 \hat{n}$  operator.

$$\begin{aligned}\langle [N]; n_2^\ell | \hat{n}^2 \hat{W}^2 + \hat{W}^2 \hat{n}^2 | [N]; n_1^\ell \rangle = & 2n_1^2 [(N - n_1)(n_1 + 2) + (N - n_1 + 1)n_1 + \ell^2] \delta_{n_2, n_1} \\ & - [n_1^2 + (n_1 - 2)^2] \sqrt{(N - n_1 + 2)(N - n_1 + 1)(n_1 + \ell)(n_1 - \ell)} \delta_{n_2, n_1 - 2} \\ & - [n_1^2 + (n_1 + 2)^2] \sqrt{(N - n_1)(N - n_1 - 1)(n_1 + \ell + 2)(n_1 - \ell + 2)} \delta_{n_2, n_1 + 2} .\end{aligned}$$

**Operator  $\hat{W}^4$**  : This operator is computed as the matrix product of the  $\hat{W}^2$  operator matrix times itself.

**Operator  $\hat{W}^2 \hat{\bar{W}}^2 + \hat{\bar{W}}^2 \hat{W}^2$**  : In this basis the only difference between the matrix elements of the  $\hat{W}^2$  and  $\hat{\bar{W}}^2$  operators is the sign of the non-diagonal contribution, which is positive in this case. The full operator is computed via matrix multiplication.

#### Appendix A.0.2. Operator Matrix Elements in the Dynamical Symmetry (II)

The diagonal operators in this dynamical symmetry are

$$SO(3) \text{ Casimir Operator } \hat{W}^2 : \langle [N]; \omega \ell | \hat{W}^2 | [N]; \omega \ell \rangle = \omega(\omega + 1).$$

$$\text{Operator } \hat{\ell}^{2q} : \langle [N]; \omega \ell | \hat{\ell}^{2q} | [N]; \omega \ell \rangle = \ell^{2q} \text{ for } q = 1, 2.$$

$$\text{Operator } \hat{\ell}^2 \hat{W}^2 : \langle [N]; \omega \ell | \hat{\ell}^2 \hat{W}^2 | [N]; \omega \ell \rangle = \ell^2 \omega(\omega + 1).$$

$$\text{Operator } \hat{W}^4 : \langle [N]; \omega \ell | \hat{W}^4 | [N]; \omega \ell \rangle = \omega^2(\omega + 1)^2.$$

The non-diagonal matrix elements in this basis are

**Operator  $\hat{n}$**  :

$$\begin{aligned}\langle [N]; w_2^\ell | \hat{n} | [N]; w_1^\ell \rangle = & \left\{ \frac{(N - w_1) [(w_1 - \ell + 2)(w_1 - \ell + 1) + (w_1 + \ell + 2)(w_1 + \ell + 1)]}{2(2w_1 + 1)(2w_1 + 3)} \right. \\ & \left. + \frac{(N + w_1 + 1) [(w_1 + \ell)(w_1 + \ell - 1) + (w_1 - \ell)(w_1 - \ell - 1)]}{2(2w_1 + 1)(2w_1 - 1)} \right\} \delta_{w_2, w_1} \\ & + \sqrt{\frac{(N - w_1)(N + w_1 + 3)(w_1 - \ell + 2)(w_1 - \ell + 1)(w_1 + \ell + 2)(w_1 + \ell + 1)}{(2w_1 + 1)(2w_1 + 3)^2(2w_1 + 5)}} \delta_{w_2, w_1 + 2} \\ & + \sqrt{\frac{(N - w_1 + 2)(N + w_1 + 1)(w_1 - \ell)(w_1 - \ell - 1)(w_1 + \ell)(w_1 + \ell - 1)}{(2w_1 - 3)(2w_1 - 1)^2(2w_1 + 1)}} \delta_{w_2, w_1 - 2}\end{aligned}$$



Note that this is the main non-diagonal operator in this case and it is again a band matrix with non-zero matrix elements located in the main and first diagonals only. The  $\hat{n}$  matrix element in this basis are taken from [29] with a typo that has been corrected.

**Operators  $\hat{n}^2$ ,  $\hat{n}^3$ , and  $\hat{n}^4$  :** These three operators are computed by matrix multiplication of the basic operator  $\hat{n}$ .

**Operator  $\hat{n}\hat{\ell}^2$  :** This operator is computed for  $\ell \neq 0$  multiplying the  $\hat{n}$  operator matrix times  $\ell^2$ .

**Operator  $\hat{n}\hat{W}^2 + \hat{W}^2\hat{n}$  :** As the operator  $\hat{n}$  is band diagonal  $\hat{W}^2$  is diagonal this operator matrix is also band diagonal with matrix elements

$$\begin{aligned} \langle [N]; w_2\ell | \hat{n}\hat{W}^2 + \hat{W}^2\hat{n} | [N]; w_1\ell \rangle = & 2\omega_1(\omega_1 + 1) \left\{ \frac{(N - w_1)[(w_1 - \ell + 2)(w_1 - \ell + 1) + (w_1 + \ell + 2)(w_1 + \ell + 1)]}{2(2w_1 + 1)(2w_1 + 3)} \right. \\ & + \left. \frac{(N + w_1 + 1)[(w_1 + \ell)(w_1 + \ell - 1) + (w_1 - \ell)(w_1 - \ell - 1)]}{2(2w_1 + 1)(2w_1 - 1)} \right\} \delta_{w_2, w_1} \\ & + [\omega_1(\omega_1 + 1) + (\omega_1 + 2)(\omega_1 + 3)] \\ & \times \sqrt{\frac{(N - w_1)(N + w_1 + 3)(w_1 - \ell + 2)(w_1 - \ell + 1)(w_1 + \ell + 2)(w_1 + \ell + 1)}{(2w_1 + 1)(2w_1 + 3)^2(2w_1 + 5)}} \delta_{w_2, w_1 + 2} \\ & + [(\omega_1 - 2)(\omega_1 - 1) + \omega_1(\omega_1 + 1)] \\ & \times \sqrt{\frac{(N - w_1 + 2)(N + w_1 + 1)(w_1 - \ell)(w_1 - \ell - 1)(w_1 + \ell)(w_1 + \ell - 1)}{(2w_1 - 3)(2w_1 - 1)^2(2w_1 + 1)}} \delta_{w_2, w_1 - 2} \end{aligned}$$

**Operator  $\hat{n}^2\hat{W}^2 + \hat{W}^2\hat{n}^2$  :** This is computed in the same way that the  $\hat{n}\hat{W}^2 + \hat{W}^2\hat{n}$  operator but taking into account that the  $\hat{n}^2$  operator is double banded. Therefore the operator matrix elements can be expressed as follow

$$\begin{aligned} \langle [N]; w_2\ell | \hat{n}^2\hat{W}^2 + \hat{W}^2\hat{n}^2 | [N]; w_1\ell \rangle = & 2\omega_1(\omega_1 + 1)[\hat{n}^2]_{w_1, w_1} \delta_{w_2, w_1} \\ & + [\omega_1(\omega_1 + 1) + (\omega_1 + 2)(\omega_1 + 3)] [\hat{n}^2]_{w_1, w_1 + 2} \delta_{w_2, w_1 + 2} \\ & + [(\omega_1 - 2)(\omega_1 - 1) + \omega_1(\omega_1 + 1)] [\hat{n}^2]_{w_1, w_1 - 2} \delta_{w_2, w_1 - 2} \\ & + [\omega_1(\omega_1 + 1) + (\omega_1 + 4)(\omega_1 + 5)] [\hat{n}^2]_{w_1, w_1 + 4} \delta_{w_2, w_1 + 4} \\ & + [(\omega_1 - 4)(\omega_1 - 3) + \omega_1(\omega_1 + 1)] [\hat{n}^2]_{w_1, w_1 - 4} \delta_{w_2, w_1 - 4} , \end{aligned}$$

where  $[\hat{n}^2]_{w_i, w_j}$  are the  $\hat{n}^2$  operator matrix elements.

**Operator  $\hat{W}^2\hat{\bar{W}}^2 + \hat{\bar{W}}^2\hat{W}^2$  :** In this basis we need first to compute the matrix elements of the  $\hat{\bar{W}}^2$  making use of Eqs. (37) and (38) of Ref. [29].



$\langle [N]; w_2 \ell_2 | \hat{R}_- | [N]; w_1 \ell_1 \rangle = A_{w_1, \ell_1} \delta_{w_2, w_1} \delta_{\ell_2, \ell_1 - 1} + B_{w_1, \ell_1} \delta_{w_2, w_1 - 2} \delta_{\ell_2, \ell_1 - 1} + C_{w_1, \ell_1} \delta_{w_2, w_1 + 2} \delta_{\ell_2, \ell_1 - 1}$  ,  
where

$$\begin{aligned} A_{w, \ell} &= \frac{(2N+3)(2\ell+1)}{(2w-1)(2w+3)} \sqrt{(w+\ell)(w-\ell+1)/2} \\ B_{w, \ell} &= -\sqrt{\frac{2(N+w+1)(N-w+2)(w+\ell)(w-\ell)(w+\ell-1)(w+\ell-2)}{(2w+1)(2w-1)^2(2w-3)}} \\ C_{w, \ell} &= \sqrt{\frac{2(N+w+3)(N-w)(w+\ell+1)(w-\ell+1)(w-\ell+2)(w-\ell+3)}{(2w+1)(2w+3)^2(2w+5)}} . \end{aligned}$$

The previous result can be used for the derivation of an expression for the  $\hat{R}_+$  operator matrix elements

$$\begin{aligned} \langle [N]; w_2 \ell_2 | \hat{R}_+ | [N]; w_1 \ell_1 \rangle^\dagger &= \langle [N]; w_1 \ell_1 | \hat{R}_+ | [N]; w_2 \ell_2 \rangle \\ &= A_{w_2, \ell_2 + 1} \delta_{w_1, w_2} \delta_{\ell_1, \ell_2 + 1} + B_{w_2 + 2, \ell_2 + 1} \delta_{w_1, w_2 - 2} \delta_{\ell_1, \ell_2 + 1} \\ &\quad + C_{w_2 - 2, \ell_2 + 1} \delta_{w_1, w_2 + 2} \delta_{\ell_1, \ell_2 + 1} . \end{aligned}$$

The upper diagonal matrix elements of the Casimir operator  $\hat{\bar{W}}^2 = \hat{R}_+ \hat{R}_- + \hat{\ell}^2$  can then be expressed as

$$\begin{aligned} \langle [N]; w_2 \ell | \hat{\bar{W}}^2 | [N]; w_1 \ell \rangle &= (A_{w_1, \ell_1}^2 + B_{w_1, \ell_1}^2 + C_{w_1, \ell_1}^2) \delta_{w_2, w_1} \\ &\quad + (A_{w_1, \ell} B_{w_1 + 2, \ell} + C_{w_1, \ell} A_{w_1 + 2, \ell}) \delta_{w_2, w_1 + 2} \\ &\quad + C_{w_1, \ell} B_{w_1 + 4, \ell} \delta_{w_2, w_1 + 4} , \end{aligned}$$

and the lower diagonal matrix elements can be computed considering that the upper and lower bandwidths are the same.

The  $\hat{W}^2 \hat{\bar{W}}^2 + \hat{\bar{W}}^2 \hat{W}^2$  operator is then computed as for the  $\hat{n}^2 \hat{W}^2 + \hat{W}^2 \hat{n}^2$  operator

$$\begin{aligned} \langle [N]; w_2 \ell | \hat{W}^2 \hat{\bar{W}}^2 + \hat{\bar{W}}^2 \hat{W}^2 | [N]; w_1 \ell \rangle &= 2\omega_1(\omega_1 + 1) [\hat{\bar{W}}^2]_{w_1, w_1} \delta_{w_2, w_1} \\ &\quad + [\omega_1(\omega_1 + 1) + (\omega_1 + 2)(\omega_1 + 3)] [\hat{\bar{W}}^2]_{w_1, w_1 + 2} \delta_{w_2, w_1 + 2} \\ &\quad + [(\omega_1 - 2)(\omega_1 - 1) + \omega_1(\omega_1 + 1)] [\hat{\bar{W}}^2]_{w_1, w_1 - 2} \delta_{w_2, w_1 - 2} \\ &\quad + [\omega_1(\omega_1 + 1) + (\omega_1 + 4)(\omega_1 + 5)] [\hat{\bar{W}}^2]_{w_1, w_1 + 4} \delta_{w_2, w_1 + 4} \\ &\quad + [(\omega_1 - 4)(\omega_1 - 3) + \omega_1(\omega_1 + 1)] [\hat{\bar{W}}^2]_{w_1, w_1 - 4} \delta_{w_2, w_1 - 4} , \end{aligned}$$

where  $[\hat{\bar{W}}^2]_{w_i, w_j}$  are the  $\hat{\bar{W}}^2$  operator matrix elements.



## References

- [1] W. Quapp, B. Winnewisser, *J. Math. Chem.* 14 (1993) 259–285.
- [2] P. Jensen, M. Spanner, P. Bunker, *J. Mol. Struct.* 1212 (2020) 128087.
- [3] W. Thorson, I. Nakagawa, *J. Chem. Phys.* 33 (1960) 994–1004.
- [4] G. Herzberg, *Molecular Spectra and Molecular Structure, Vol. III: Electronic Spectra and Electronic Structure of Polyatomic Molecules*, Van Nostrand Reinhold, New York, 1966.
- [5] R. N. Dixon, *Trans. Faraday Soc.* 60 (1964) 1363–1368.
- [6] J. T. Hougen, P. Bunker, J. Johns, *J. Mol. Spectrosc.* 34 (1970) 136–172.
- [7] P. Bunker, B. Landsberg, *J. Mol. Spectrosc.* 67 (1977) 374 – 385.
- [8] S. Ross, *J. Mol. Spectrosc.* 132 (1988) 48 – 79.
- [9] P. Jensen, *J. Mol. Spectrosc.* 128 (1988) 478–501.
- [10] L. Bates, *Zeitschrift für angewandte Mathematik und Physik* 42 (1991) 837 – 847.
- [11] M. S. Child, *J. Phys. A: Math. and General* 31 (1998) 657–670.
- [12] M. S. Child, T. Weston, J. Tennyson, *Mol. Phys.* 96 (1999) 371–379.
- [13] B. Winnewisser, M. Winnewisser, I. Medvedev, M. Behnke, F. De Lucia, S. Ross, J. Koput, *Phys. Rev. Lett.* 95 (2005) 243002.
- [14] N. Zobov, S. Shirin, O. Polyansky, J. Tennyson, P.-F. Coheur, P. Bernath, M. Carleer, R. Colin, *Chem. Phys. Lett.* 414 (2005) 193 – 197.
- [15] M. Winnewisser, B. Winnewisser, I. Medvedev, F. D. Lucia, S. Ross, L. Bates, *J. Mol. Struct.* 798 (2006) 1 – 26.
- [16] B. Winnewisser, M. Winnewisser, I. Medvedev, F. De Lucia, S. Ross, J. Koput, *Phys. Chem. Chem. Phys.* 12 (2010) 8158–8189.
- [17] N. Reilly, P. Changala, J. Baraban, D. Kokkin, J. Stanton, M. McCarthy, *J. Chem. Phys.* 142 (2015) 231101.
- [18] F. Iachello, *Lie Algebras and Applications (Lecture Notes in Physics)*, Vol. 708, Springer, Berlin, 2006.
- [19] F. Iachello, A. Arima, *The Interacting Boson Model*, Cambridge University Press, Cambridge, 1987.
- [20] F. Iachello, *Rev. Mod. Phys.* 65 (1993) 569–576.
- [21] R. Bijker, F. Iachello, A. Leviatan, *Ann. Phys.* 236 (1994) 69 – 116.



- [22] F. Iachello, R. Levine, Algebraic Theory of Molecules, Oxford University Press, New York, 1995.
- [23] F. Iachello, Chem. Phys. Lett. 78 (1981) 581 – 585.
- [24] O. V. Roosmalen, A. Dieperink, F. Iachello, Chem. Phys. Lett. 85 (1982) 32 – 36.
- [25] F. Iachello, S. Oss, R. Lemus, J. Mol. Spectrosc. 149 (1991) 132 – 151.
- [26] F. Iachello, S. Oss, J. Chem. Phys. 104 (1996) 6956–6963.
- [27] F. Iachello, F. Pérez-Bernal, P. Vaccaro, Chem. Phys. Lett. 375 (2003) 309 – 320.
- [28] F. Pérez-Bernal, L. Santos, P. Vaccaro, F. Iachello, Chem. Phys. Lett. 414 (2005) 398 – 404.
- [29] F. Pérez-Bernal, F. Iachello, Phys. Rev. A 77 (2008) 032115.
- [30] R. Gilmore, J. Math. Phys. 20 (1979) 891–893.
- [31] P. Cejnar, J. Jolie, Prog. Part. Nucl. Phys. 62 (2009) 210 – 256.
- [32] R. Casten, Prog. Part. Nucl. Phys. 62 (2009) 183 – 209.
- [33] P. Cejnar, J. Jolie, R. Casten, Rev. Mod. Phys. 82 (2010) 2155–2212.
- [34] Y. Zhang, F. Pan, Y.-X. Liu, J. Draayer, J. Phys. B – At. Mol. Opt. 43 (2010) 225101.
- [35] P. Pérez-Fernández, J. Arias, J. E. García-Ramos, F. Pérez-Bernal, Phys. Rev. A 83 (2011) 062125.
- [36] M. Calixto, E. Romera, R. del Real, J. Phys. A: Math. Theor. 45 (2012) 365301.
- [37] M. Calixto, R. del Real, E. Romera, Phys. Rev. A 86 (2012) 032508.
- [38] F. de los Santos, E. Romera, Phys. Rev. A 87 (2013) 013424.
- [39] O. Castaños, M. Calixto, F. Pérez-Bernal, E. Romera, Phys. Rev. E 92 (2015) 052106.
- [40] P. Cejnar, M. Macek, S. Heinze, J. Jolie, J. Dobeš, J. Phys. A: Math. and General 39 (2006) L515–L521.
- [41] M. Caprio, P. Cejnar, F. Iachello, Annals of Physics 323 (2008) 1106 – 1135.
- [42] P. Pérez-Fernández, A. Relaño, J. M. Arias, P. Cejnar, J. Dukelsky, J. E. García-Ramos, Phys. Rev. E 83 (2011) 046208.



- [43] V. Bastidas, P. Pérez-Fernández, M. Vogl, T. Brandes, Phys. Rev. Lett. 112 (2014) 140408.
- [44] P. Pérez-Fernández, A. Relaño, J. M. Arias, J. Dukelsky, J. E. García-Ramos, Phys. Rev. A 80 (2009) 032111.
- [45] Z.-G. Yuan, P. Zhang, S.-S. Li, J. Jing, L.-B. Kong, Phys. Rev. A 85 (2012) 044102.
- [46] T. Brandes, Phys. Rev. E 88 (2013) 032133.
- [47] M. Kloc, P. Stránský, P. Cejnar, J. Phys. A: Math. and Theor. 50 (2017) 315205.
- [48] F. Pérez-Bernal, O. Álvarez-Bajo, Phys. Rev. A 81 (2010) 050101.
- [49] F. Pérez-Bernal, L. Santos, Fortschritte der Physik 65 (2017) 1600035.
- [50] D. Larese, F. Iachello, J. Mol. Struct. 1006 (2011) 611 – 628.
- [51] D. Larese, F. Pérez-Bernal, F. Iachello, J. Mol. Struct. 1051 (2013) 310 – 327.
- [52] B. Dietz, F. Iachello, M. Miski-Oglu, N. Pietralla, A. Richter, L. von Smekal, J. Wambach, Phys. Rev. B 88 (2013) 104101.
- [53] L. Zhao, J. Jiang, T. Tang, M. Webb, Y. Liu, Phys. Rev. A 89 (2014) 023608.
- [54] J. Khalouf-Rivera, M. Carvajal, L. Santos, F. Pérez-Bernal, J. Phys. Chem. A 123 (2019) 9544–9551.
- [55] F. Evers, A. Mirlin, Rev. Mod. Phys. 80 (2008) 1355–1417.
- [56] L. Santos, F. Pérez-Bernal, Phys. Rev. A 92 (2015) 050101.
- [57] L. Santos, M. Távora, F. Pérez-Bernal, Phys. Rev. A 94 (2016) 012113.
- [58] A. E. L. Dieperink, O. Scholten, F. Iachello, Phys. Rev. Lett. 44 (1980) 1747–1750.
- [59] A. Leviatan, M. Kirson, Ann. Phys. 188 (1988) 142 – 185.
- [60] S. Oss, M. A. Tamsamani, J. Chem. Phys. 108 (1998) 1773–1779.
- [61] M. Abbouti Tamsamani, J.-M. Champion, S. Oss, J. Chem. Phys. 110 (1999) 2893–2902.
- [62] T. Sako, D. Aoki, K. Yamanouchi, F. Iachello, J. Chem. Phys. 113 (2000) 6063–6069.
- [63] H. Ishikawa, H. Toyosaki, N. Mikami, F. Pérez-Bernal, P. Vaccaro, F. Iachello, Chem. Phys. Lett. 365 (2002) 57 – 68.



- [64] M. Sánchez-Castellanos, R. Lemus, M. Carvajal, F. Pérez-Bernal, J. Fernández, *Chem. Phys. Lett.* 554 (2012) 208 – 213.
- [65] R. Lemus, M. Sánchez-Castellanos, F. Pérez-Bernal, J. M. Fernández, M. Carvajal, *J. Chem. Phys.* 141 (2014) 054306.
- [66] M. Bermúdez-Montaña, M. Carvajal, F. Pérez-Bernal, R. Lemus, *J. Raman Spectrosc.* 51 (2020) 569–583.
- [67] M. Rodríguez-Arcos, R. Lemus, *Chem. Phys. Lett.* 713 (2018) 266 – 271.
- [68] M. M. Estévez-Fregoso, R. Lemus, *Mol. Phys.* 116 (2018) 2374–2395.
- [69] M. M. Estévez-Fregoso, J. M. Arias, J. Gómez-Camacho, R. Lemus, *Mol. Phys.* 116 (2018) 2254–2269.
- [70] J. Baraban, P. Changala, G. Mellau, J. Stanton, A. Merer, R. Field, *Science* 350 (2015) 1338–1342.
- [71] F. Iachello, F. Pérez-Bernal, *Mol. Phys.* 106 (2008) 223.
- [72] F. Pérez-Bernal, L. Fortunato, *Phys. Lett. A* 376 (2012) 236–244.
- [73] F. Iachello, F. Pérez-Bernal, *J. Phys. Chem. A* 113 (2009) 13273–13286.
- [74] D. Larese, M. Caprio, F. Pérez-Bernal, F. Iachello, *J. Chem. Phys.* 140 (2014) 014304.
- [75] M. Calixto, F. Pérez-Bernal, *Phys. Rev. A* 89 (2014) 032126.
- [76] F. Iachello, B. Dietz, M. Miski-Oglu, A. Richter, *Phys. Rev. B* 91 (2015) 214307.
- [77] A. Frank, P. V. Isacker, *Algebraic Methods in Molecular and Nuclear Structure Physics*, John Wiley and Sons, New York, 1994.
- [78] V. Zelevinsky, B. Brown, N. Frazier, M. Horoi, *Phys. Rep.* 276 (1996) 85 – 176.
- [79] F. Izrailev, *Phys. Rep.* 196 (1990) 299 – 392.
- [80] E. Anderson, Z. Bai, C. Bischof, S. Blackford, J. Demmel, J. Dongarra, J. Du Croz, A. Greenbaum, S. Hammarling, A. McKenney, D. Sorensen, *LAPACK Users’ Guide*, 3rd Edition, Society for Industrial and Applied Mathematics, Philadelphia, PA, 1999.
- [81] V. Barker, L. S. Blackford, et al., *Lapack95 users’ guide*, Tech. rep., Netlib.org (2001).
- [82] F. James, M. Roos, *Computer Physics Communications* 10 (6) (1975) 343–367.



- [83] J. Khalouf-Rivera, M. Carvajal, F. Pérez-Bernal, The 2DVMU3 program suite, in preparation.
- [84] E. B. Wilson, J. C. Decius, P. C. Cross, *Molecular Vibrations: The Theory of Infrared and Raman Vibrational Spectra*, Mc Graw-Hill Book Company, INC., 1955.
- [85] G. Schulze, O. Koja, B. Winnewisser, M. Winnewisser, *J. Mol. Struct.* 517 (2000) 307–325.
- [86] F. Winther, *J. Mol. Spectrosc.* 62 (1976) 232–246.
- [87] I. Kozin, R. Roberts, *J. Chem. Phys.* 118 (2003) 10523–10533.
- [88] K. Efstathiou, M. Joyeux, D. A. Sadovskii, *Phys. Rev. A* 69 (2004) 032504.
- [89] G. Mellau, *J. Chem. Phys.* 134 (2011) 234303.
- [90] J. Bowman, B. Gazdy, J. Bentley, T. Lee, C. Dateo, *J. Chem. Phys.* 99 (1993) 308–323.
- [91] G. Mellau, *J. Chem. Phys.* 133 (2010) 164303.
- [92] P. Bunker, J. Stone, *J. Mol. Spectrosc.* 41 (2) (1972) 310 – 332.
- [93] H. Lichau, S. Ross, M. Lock, S. Albert, B. Winnewisser, M. Winnewisser, F. De Lucia, *J. Phys. Chem. A* 105 (2001) 10080–10088.
- [94] O. Álvarez-Bajo, M. Carvajal, F. Pérez-Bernal, *Chem. Phys.* 392 (1) (2012) 63 – 70.
- [95] M. Carvajal, R. Lemus, *The Journal of Physical Chemistry A* 119 (2015) 12823–12838.
- [96] I. Kozin, P. Jensen, *J. Mol. Spectrosc.* 163 (1994) 483–509.
- [97] L. Halonen, T. Carrington, *J. Chem. Phys.* 88 (1988) 4171.
- [98] I. Tokue, K. Yamasaki, S. Nanbu, *J. Chem. Phys.* 122 (2005) 144307.
- [99] V. Tyuterev, S. Tashkun, D. Schwenke, P. Jensen, T. Cours, A. Barbe, M. Jacon, *Chem. Phys. Lett.* 316 (2000) 271 – 279.
- [100] O. Polyansky, P. Jensen, J. Tennyson, *J. Mol. Spectroscopy* 178 (1996) 184–188.
- [101] O. Ulenikov, A. Malikova, M. Koivusaari, S. Alanko, R. Anttila, *J. Mol. Spectrosc.* 176 (2) (1996) 229 – 235.
- [102] L. Brown, J. Crisp, D. Crisp, O. Naumenko, M. Smirnov, L. Sinita, A. Perrin, *J. Mol. Spectrosc.* 188 (2) (1998) 148 – 174.



- [103] O. Ulenikov, A.-W. Liu, E. Bekhtereva, O. Gromova, L.-Y. Hao, S.-M. Hu, *J. Mol. Spectrosc.* 234 (2005) 270 – 278.
- [104] A. Azzam, S. Yurchenko, J. Tennyson, M.-A. Martin-Drumel, O. Pirali, *J. Quant. Spectrosc. Rad. Trans.* 130 (2013) 341 – 351.
- [105] P. Jensen, I. Kozin, *Journal of molecular spectroscopy* 160 (1993) 39–57.
- [106] J. Senekowitsch, A. Zilch, S. Carter, H.-J. Werner, P. Rosmus, P. Botschwina, *Chem. Phys.* 122 (1988) 375.
- [107] E. Kauppi, L. Halonen, *J. Phys. Chem.* 94 (1990) 5779.
- [108] E. Palik, R. A. Oetjen, *J. Mol. Spectrosc.* 1 (1) (1957) 223 – 238.
- [109] E. Palik, *J. Mol. Spectrosc.* 3 (1959) 259 – 295.
- [110] J. Gillis, T. Edwards, *J. Mol. Spectrosc.* 85 (1981) 74 – 84.
- [111] J. Flaud, C. Camypeyret, H. Burger, H. Willner, *J. Mol. Spectrosc.* 161 (1) (1993) 157 – 169.
- [112] J.-M. Flaud, C. Camy-Peyret, P. Arcas, H. Bürger, H. Willner, *J. Mol. Spectrosc.* 167 (1994) 383–399.
- [113] H. Ishikawa, Y. Muramoto, N. Mikami, *J. Mol. Spectrosc.* 216 (2002) 9097.
- [114] C. Yamada, H. Kanamori, E. Hirota, N. Nishiwaki, N. Itabashi, K. Kato, T. Goto, *J. Chem. Phys.* 91 (1989) 45824586.
- [115] H. Ishikawa, O. Kajimoto, *J. Mol. Spectrosc.* 150 (1991) 610619.
- [116] E. Hirota, H. Ishikawa, *J. Chem. Phys.* 110 (1999) 4254–4257.
- [117] S. Yurchenko, P. Bunker, W. Kraemer, P. Jensen, *Can. J. Chem.* 82 (2004) 694.
- [118] V. Clark, A. O. J. Tennyson, S. Yurchenko, *J. Quant. Spectr. Rad. Transf.* 246 (2020) 106929.
- [119] H. Pickett, E. Cohen, L. Brown, C. Rinsland, M. Smith, V. Malathy-Devi, A. Goldman, A. Barbe, B. Carli, M. Carlotti, *J. Mol. Spectrosc.* 128 (1988) 151–171.
- [120] F. Pérez-Bernal, J. Arias, A. Frank, R. Lemus, R. Bijker, *J. Mol. Spectrosc.* 184 (1997) 1–11.
- [121] A. Barbe, S. Mikhailenko, J. Plateaux, *J. Mol. Spectrosc.* 184 (1997) 448–453.
- [122] A. Barbe, A. Chichery, V. Tyuterev, S. Tashkun, S. Mikhailenko, *Spectrochimica Acta A* 54 (1998) 1935–1945.



- [123] S. Mikhailenko, A. Barbe, V. Tyuterev, *J. Mol. Spectrosc.* 215 (2002) 29–41.
- [124] J.-M. Colmont, B. Bakri, J. Demaison, H. Mader, F. Willaert, V. Tyuterev, A. Barbe, *J. Mol. Spectrosc.* 233 (2005) 293–296.
- [125] Y. Babikov, S. Mikhailenko, A. Barbe, V. Tyuterev, *J. Quant. Spectrosc. Radiat. Transfer* 145 (2014) 169–196.
- [126] M. Bermúdez-Montaña, R. Lemus, *J. Mol. Spectrosc.* 331 (2017) 89–105.
- [127] J. Koput, *J. Mol. Spectrosc.* 115 (1986) 131–146.
- [128] S. Ross, M. Niedenhoff, K. Yamada, *J. Mol. Spectr.* 164 (1994) 432–444.
- [129] M. Niedenhoff, G. Winnewisser, K. Yamada, S. Belov, *J. Mol. Spectrosc.* 169 (1995) 224–242.
- [130] H. Lichau, C. Gillies, J. Gillies, S. Ross, B. Winnewisser, M. Winnewisser, *J. Phys. Chem. A* 105 (2001) 10065–10079.
- [131] J. Koput, *Chem. Phys. Lett.* 320 (2000) 237–244.
- [132] M. McCarthy, J. Baraban, P. Changala, J. Stanton, M.-A. Martin-Drumel, S. Thorwirth, C. Gottlieb, N. Reilly, *J. Phys. Chem. Lett.* 6 (2015) 2107–2111.
- [133] B. McGuire, M.-A. Martin-Drumel, S. Thorwirth, S. Brünken, V. Lattanzi, J. Neill, S. Spezzano, Z. Yu, D. Zaleski, A. Remijan, B. Pate, M. McCarthy, *Phys. Chem. Chem. Phys.* 18 (2016) 22693–22705.
- [134] M. Niedenhoff, K. Yamada, G. Winnewisser, *J. Mol. Spectrosc.* 183 (1997) 176–199.
- [135] M. King, H. Kroto, B. Landsberg, *J. Mol. Spectr.* 113 (1985) 1–20.
- [136] J. Lolck, S. Brodersen, *J. Mol. Spectr.* 72 (1978) 445–462.
- [137] L. Fusina, I. Mills, *J. Mol. Spectrosc.* 79 (1980) 123–131.
- [138] J. VanderAuwera, J. Johns, O. Polyansky, *J. Chem. Phys.* 95 (4) (1991) 2299–2316.
- [139] C. Rittby, *J. Chem. Phys.* 95 (1991) 56095611.
- [140] J. Presilla-Márquez, W. Graham, *J. Chem. Phys.* 95 (1991) 56125617.
- [141] J. Koput, *J. Mol. Spectr.* 342 (2017) 83–91.